Foehn Winds at Pine Island Glacier and their role in Ice Changes

Diana Francis[1*], Ricardo Fonseca[1], Kyle S. Mattingly[2], Stef Lhermitte[3,5], Catherine Walker[4]

[1] The Environmental and Geophysical Sciences (ENGEOS) Lab, Khalifa University, P. O. Box 127788, Abu Dhabi, United Arab Emirates.
[2] Space Science and Engineering Center, University of Wisconsin-Madison, Madison, WI, USA.
[3] Department of Earth & Environmental Sciences, KU Leuven, Belgium.
[4] Department of Applied Ocean Physics and Engineering, Woods Hole Oceanographic Institution, Woods Hole, MA, USA.
[5] Department of Geosciences & Remote Sensing, Delft University of Technology, Netherlands.

*Corresponding author: diana.francis@ku.ac.ae

Abstract

Pine Island Glacier (PIG) has recently experienced increased ice loss mostly attributed to basal melt and ocean-ice dynamics. However, atmospheric forcing also plays a role in the ice mass budget, as besides lower-latitude warm air intrusions, the steeply sloping terrain that surrounds the glacier promotes frequent Foehn winds. An investigation of 41-years of reanalysis data reveals that Foehn occurs more frequently from June to October, with Foehn episodes typically lasting about 5 to 9 h. An analysis of the surface mass balance indicated that their largest impact is on the surface sublimation, which is increased by about 1.4 mm water equivalent (w.e.) day^{-1} with respect to no-Foehn events. Blowing snow makes roughly the same contribution as snowfall, around 0.34-0.36 mm w.e. day^{-1}, but with the opposite sign. The melting rate is three orders of magnitude smaller than the surface sublimation rate. The negative phase of the Antarctic Oscillation and the positive phase of the Southern Annular Mode promote the occurrence of Foehn at PIG. A particularly strong event took place on 09-11 November 2011, when 10-m winds speeds in excess of 20 m s^{-1} led to downward sensible heat fluxes higher than 75 W m^{-2} as they descended the mountainous terrain. Surface sublimation and blowing snow sublimation dominated the surface mass balance, with magnitudes of up to 0.13 mm w.e. hr^{-1}. Satellite data indicated an hourly surface melting area exceeding 100 km^2. Our results stress the importance of the atmospheric forcing on the ice mass balance at PIG.

Keywords: Pine Island Glacier, Foehn Winds, Amundsen Sea Low, Snow Sublimation, Surface Mass Balance, Ice Loss.

1. Introduction

The West Antarctic Ice Sheet and its marine terminating ice shelves have been thinning rapidly in the last few decades, contributing to roughly 10% of the observed global mean sea-level rise (Jenkins et al., 2010; Smith et al., 2020). A collapse of the West Antarctic Ice Sheet alone is estimated to lead to a 3 m rise in the global sea-level (Bamber et al., 2009b), and model simulations suggest it can be initiated by an ocean warming of approximately 1.2ºC (Rosier et al., 2021). One of the main contributors to the ice loss in West Antarctica is Pine Island Glacier (PIG), Fig. 1a, which is presently Antarctica's single largest contributor to sea-level rise (Favier et al., 2014; Joughin et al., 2021; Lhermitte et al., 2021). Over the last two decades PIG has lost more than a trillion tons of ice, which corresponds to a roughly 3 mm rise in sea-level (De Rydt et al., 2021). Satellite images indicate a jump in the average volume loss rate around PIG from roughly $2.6\,\mathrm{km}^3$ y^{-1} in 1995 to $10.1\,\mathrm{km}^3\mathrm{y}^{-1}$ in 2006 (Wingham et al., 2009), with recent studies stressing a further speedup of ice loss since 2017 (Joughin et al., 2021; Lhermitte et al., 2021; Nilsson et al., 2022). In fact, Li et al. (2022) reported a decrease in elevation around PIG, as estimated from satellite measurements, at a rate of approximately $-2 \pm 0.04\,\mathrm{m}\,\mathrm{y}^{-1}$ from 2016 to 2019. Satellite data indicates an ice velocity magnitude in excess of $200\,\mathrm{m}\,\mathrm{y}^{-1}$ over a broad region, Fig. 1a, with peak values higher than $4.5\,\mathrm{km}\,\mathrm{y}^{-1}$ (Liu et al., 2022). The ice loss at PIG can be seen by the rapid retreat of the ice front, Fig. 1b, in particular since 2015, with major calving events taking place in October-November 2018 and February 2020 (Liu et al., 2022; Lhermitte et al., 2021).

(a)
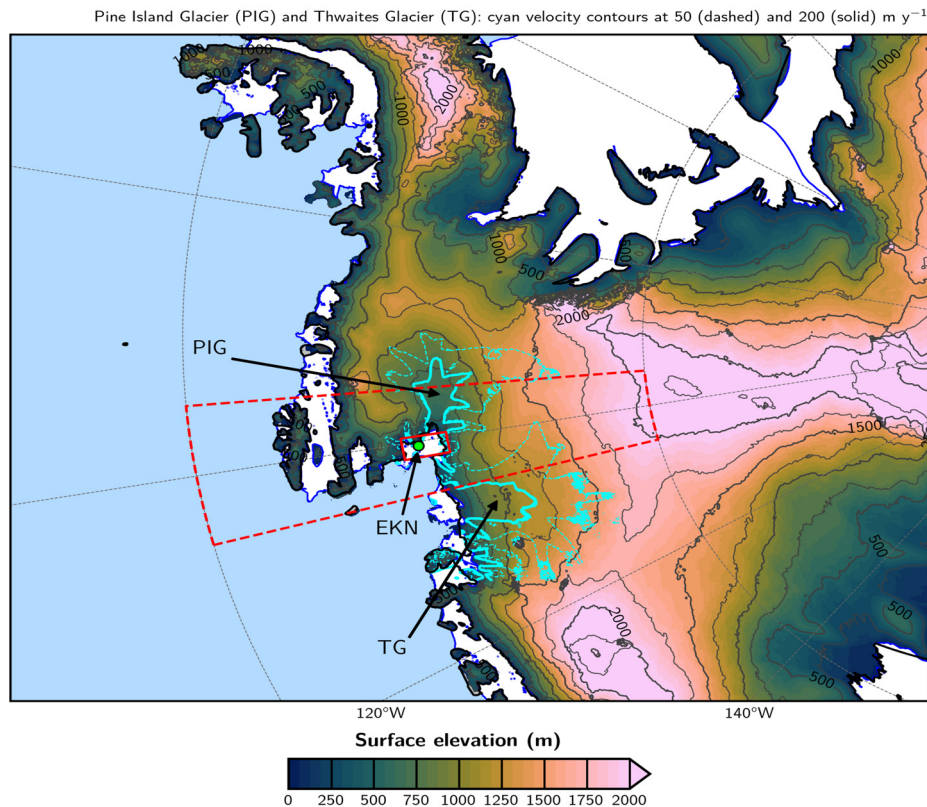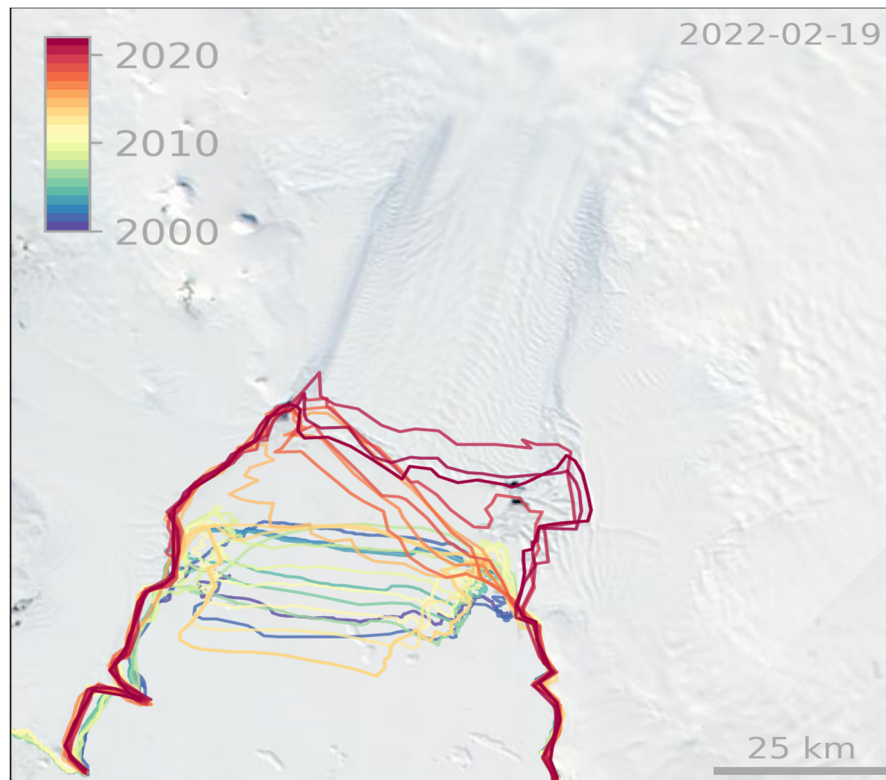
Figure 1: **Pine Island Glacier (PIG) and surroundings:** (a) Digital elevation map (DEM) at 1 km resolution, constructed using data for March 1994-January 1995 and February 2003-March 2008, showing PIG and the Thwaites Glacier (TG). The shading and the black contours show the surface elevation (m), contoured every 500 m and labelled every 1,000 m, while the regions where the ice velocity is equal to $50\,\mathrm{m\,y^{-1}}$ and $200\,\mathrm{m\,y^{-1}}$ are denoted by the dashed and solid cyan contours, respectively. The ice velocities are estimated using data from the National Snow and Ice Data Center (NSIDC; Rignot et al., 2017) for 1996-2016. The blue line highlights the ice shelves borders. The solid red rectangle represents the domain over which the averaging is performed for the time series in Fig. 7 (-101.5ºW to -99.5ºW; -75.5ºS to -74.5ºS), whereas the dashed red rectangle highlights the domain used in Figs. 3-4 (105ºW to 95ºW; 80ºS to 70ºS). The location of the Evans Knoll weather station (-74.85ºS; -100.404ºW) is given by the green circle. (b) 19 February 2022 MODIS satellite image of PIG with an overlay of historical calving fronts since 2000.

56

57   The melting around PIG has been attributed mostly to basal melt and ocean-ice dynamics (
58   Weber et al., 2017; De Rydt et al, 2021; Joughin et al., 2021). While ocean dynamics likely account
59   for most of the observed ice loss, atmospheric forcing may also be important in modulating PIG
60   ice loss, as is it has been shown recently to be the case elsewhere in the continent (e.g. Francis et
61   al. 2021, 2022; Greene et al., 2022). Besides atmospheric rivers (Willie et al., 2021; Francis et al.,
62   2020) and associated surface radiative warming, one of the meteorological phenomena that can
63   foster ice damage around Antarctica is Foehn winds (Elvidge and Renfrew, 2016; Ghiz et al. 2021).
64   The word Foehn, which means "hair dryer" in German, refers to the warm and dry winds that
65   descend on the leeside of a mountain range. Foehn effects can trigger surface melting and snow or
66   ice sublimation (Bell et al., 2018), with melting less likely as the low humidities during Foehn
67   episodes cause large latent heat losses from the snowpack and hence prevent its warming.
68   Additionally, Foehn winds can foster calving events (Miles et al., 2017), as an offshore wind

69 direction, combined with ocean swells, aids in the breakup and subsequent drifting of newly
70 formed icebergs (Francis et al., 2022).
71

72 Several studies have reported the occurrence of Foehn around Antarctica such as in the Ross
73 Sea (e.g., Speirs et al., 2013; Zou et al. 2021a, b), PIG (Djoumna and Holland, 2021), Vestfold
74 Hills in East Antarctica (Gehring et al., 2022) and Antarctic Peninsula (e.g., Laffin et al., 2021).
75 Zou et al. (2021a, b) investigated the processes behind four major melting events at the Ross Ice
76 Shelf. In three of the four cases Foehn warming occurred for more than 40% of the melting period,
77 causing a 2-4°C increase in surface temperature. The authors concluded that Foehn can be an
78 important contributor to surface melting in Antarctica, which can increase the effects of warm and
79 moist air advection. Djoumna and Holland (2021) reported Foehn conditions around PIG during
80 March 2013 after the onset of a warm air intrusion associated with an atmospheric river. The
81 combination of warm and moist air advection from lower latitudes and Foehn winds likely explains
82 the record temperature of 17.5°C observed at the northern tip of the Antarctic Peninsula on 24
83 March 2015 (Bozkurt et al., 2018). A region in Antarctica particularly prone to Foehn effects is
84 the McMurdo Dry Valleys. Speirs et al. (2013) presented a 20-year climatology of Foehn events
85 at this site from weather station data. They reported positive trends for all seasons during 1999-
86 2008 with a larger magnitude in winter when the large-scale dynamics favour the occurrence of
87 Foehn. The role of Foehn winds in the disintegration and collapse of the Larsen ice shelves A, B
88 and C on the Antarctic Peninsula in 1995, 2002 and 2017 respectively, has been widely reported (
89 Massom et al., 2018). In fact, during periods of strong westerlies, the warmer and more moist
90 maritime air is forced to rise over the mountains in the western Antarctic Peninsula and warms and
91 dries out on the leeside, generating frequent Foehn events over the ice shelves on the eastern side
92 of the peninsula (Laffin et al., 2021). The complex terrain around PIG (Fig. 1a) favours Foehn
93 wind occurrence there as well.
94

95 Despite major advances in the understanding of the Antarctic surface mass balance in recent
96 decades, there are still major uncertainties (e.g. The IMBIE team, 2018) in particular in areas that
97 are prone to ice loss such as PIG (Kowalewski et al., 2021). An important process for the surface
98 mass balance is snow evaporation or sublimation (Das et al., 2013; Mottram et al., 2021), which
99 is typically difficult to detect from observations given its nature. Even though Foehn events are
100 believed to play an important role in the surface mass loss around Antarctica (Ghiz et al., 2021),
101 the underlying processes remain unclear. Moreover, no study has examined the occurrence of
102 Foehn on a longer time-scale over PIG, even though it is expected to have a significant impact
103 given the steep topography in the region (Fig. 1a). Hence, it is vital to quantify the occurrence of
104 Foehn episodes so as to better understand their role in ice loss through melting and/or sublimation.
105 This is achieved in the present work, where the occurrence of Foehn at PIG and its role in the
106 surface mass balance is investigated using a state-of-the-art reanalysis dataset, satellite imagery
107 and in situ measurements.
108

109   The remainder of the paper is organised as follows. In section 2, the datasets used in this work
110 as well as the Foehn-detection algorithm employed and how the different terms in the surface mass
111 balance are quantified are described. Section 3 provides a discussion of the occurrence and trends
112 of Foehn over PIG, as well as its impacts on the surface mass balance. In Section 4 the focus is on
113 the large-scale conditions that promote the occurrence of Foehn, while a case study in November
114 2011 is discussed in section 5. Section 6 summarises the main findings of the study.
115

2. Datasets and Methodology

2.1. Observational and Reanalysis Datasets

118   The main dataset used in this study is the ERA-5 reanalysis data (Hersbach et al., 2020),
119 which is available on an hourly basis and on a 0.25º × 0.25º (~27 km) grid from 1950 to present.
120 Both hourly pressure-level (Hersbach et al., 2018a) and surface (Hersbach et al., 2018b) data
121 are considered in this work for the period 1980-2020. ERA-5 is one of the best performing
122 reanalysis datasets around Antarctica in comparison with station observations as noted e.g. by
123 Gossart et al. (2019).

124   The 1 km × 1 km dataset used for the Digital Elevation Model of Pine Island Glacier (PIG)
125 and surrounding region combines measurements collected by the European Remote Sensing
126 Satellite-1 (ERS-1) Satellite Radar Altimeter from March 1994 to January 1995, and the Ice,
127 Cloud, and land Elevation Satellite (ICESat) Geosciences Laser Altimeter System from
128 February 2003 to March 2008 (Bamber et al., 2009b). The ice velocity for PIG and Thwaites
129 Glacier is estimated from a combination of satellite interferometric and synthetic-aperture radar
130 systems, and is available at a 450 m spatial resolution from 1996 to 2016 (Rignot et al., 2016).
131 Sentinel 2 satellite data, downloaded from Copernicus website (Copernicus, 2022), is used to
132 extract the sea-ice front at PIG for 2000-2022.

133   Surface radiation fluxes from the Clouds and Earth's Radiant Energy System (CERES;
134 Doelling et al. 2013, 2016) dataset are available on an hourly basis at 1º × 1º resolution from
135 March 2000 to present. The CERES product used here is the SYN1deg - Level 3, which is freely
136 available online (NASA/LARC/SD/ASDC, 2017), and is downloaded for the period 03-14
137 November 2011 that corresponds to the case study discussed in section 5.
138

139   10-min air temperature observations at the Evans Knoll station (-74.85ºS, -100.404ºW; 188
140 m above sea-level), located just to the northeast of PIG (green circle in Fig. 1a), are freely
141 available at the Antarctic Meteorological Research Center & Automatic Weather Stations
142 Project website, Space Science and Engineering Center, University of Wisconsin-Madison
143 (Lazzara et al., 2022). This data is extracted for the case study (03-14 November 2011)
144 considered in this work.

The surface melt area, for the period 03-14 November 2011, is estimated using measurements collected by the Moderate Resolution Imaging Spectroradiometer (MODIS; Kaufman et al., 1997) on board the National Aeronautic and Space Administration's Terra and Aqua satellites. In particular, the daily global surface reflectance Level 3 data at 0.05º × 0.05º spatial resolution (MODIS products MOD09CMG and MYD09CMG for Terra and Aqua, respectively; Vermote 2015a,b) is downloaded, and the enhanced Normalised Difference Water Index (NDWI) defined in Moussavi et al. (2016) is estimated. The NDWI index makes use of the reflectance contrast between water and ice in the red (630-690 nm) and blue (450-510 nm) bands.

2.2. Foehn-Detection Algorithm

Foehn events at PIG are identified using a modified version of the algorithm proposed by Laffin et al. (2021), in which the authors studied Foehn episodes in the Antarctic Peninsula using ERA-5, model and observational data. A given hourly time-step is denoted as a Foehn time-step if the following three conditions hold:

$$\begin{cases} 2m\ Temperature > 60^{th}\ Percentile \\ 2m\ Relative\ Humidity < 30^{th}\ Percentile \\ 10m\ Wind\ Speed > 60^{th}\ Percentile \end{cases} \quad (1)$$

where the temperature, relative humidity (RH) and wind speed are extracted from ERA-5, and the algorithm is applied in a 10º × 10º domain (105º-95ºW, 80º-70ºS) centered on PIG. The thresholds are grid-point dependent, and while the RH and wind speed thresholds are computed over the full 40-year period (1980-2020), hourly thresholds for each month are used for the air temperature to account for the annual cycle. Laffin et al. (2021) used a threshold of 0ºC for the temperature as the focus was on Foehn events that cause surface melt. However, such a threshold is hardly met at PIG (Moncada and Holland, 2019; Djoumna and Holland, 2021) given its poleward location compared to the Antarctic Peninsula (~75ºS vs. ~60º-70ºS) and resulting reduced exposure to the warmer lower-latitude air. It is important to note, however, that a surface or air temperature above 0ºC is not needed for surface melting to take place. As noted by Ghiz et al. (2021), melting can occur at surface and air temperatures below freezing provided the melt energy, given by the sum of the surface radiation, turbulent and ground heat fluxes, is positive for at least two diurnal cycles. In addition to melting, Foehn promotes snow sublimation (Kirchgaessner et al., 2021) and depletes firn air content from ice shelves, which encourages meltwater-induced hydrofracture (Bell et al., 2018). Given this, the 60th percentile of the air temperature is used as the temperature threshold instead, in line with that considered for the wind speed but taking into account the strong annual variability in the region. The threshold values range from about 2 to 12 m s^{-1} for the 10-m wind speed, 232 K to 274 K for the 2-m air temperature, and 59 to 82% for the 2-m relative humidity.

It is important to note that ERA-5 reanalysis data lacks the spatial resolution to properly resolve smaller-scale flows, and therefore may not give a full picture of Foehn around PIG. However, the findings of Laffin et al. (2021) suggest that its representation of Foehn, at least in the Antarctic Peninsula, is accurate enough in particular for moderate and strong episodes to justify its use here. In particular, these authors found that the reanalysis captured roughly 92% of the Foehn events detected with in situ weather station data. The biases in the ERA-5 radiative fluxes, which in a comparison with in situ observations at Siple Dome next to the Ross Ice Shelf are as large as $100\,\mathrm{W\,m^{-2}}$ for the downward shortwave and $50\,\mathrm{W\,m^{-2}}$ for the downward longwave (Ghiz et al., 2021), suggest that a Foehn identification algorithm based on the surface energy budget, and using ERA-5 data, may not be optimal for Antarctica. The reanalysis performance in terms of 2-m temperature, relative humidity and 10-m wind speed, the fields used in the Foehn detection algorithm (1), is superior, with typical biases of 0.5-1.5ºC, 5-10% and 0.5-1.5 $\mathrm{m\,s^{-1}}$, respectively, as noted by Gossart et al. (2019).

2.3. Surface Mass Balance

Over snowy regions such as Antarctica, and following Dery and Yau (1999, 2002) and Scarchilli et al. (2010), the surface mass balance can be expressed as

$$S = P - E - M - Q_{snow} - D \quad (2)$$

where S is the rate of accumulation or storage of snow at the surface, P is the precipitation (snowfall) rate, E is the surface evaporation rate which includes the sublimation rate (Q_{surf}), M represents the surface melt and runoff rate, Q_{snow} is the blowing snow sublimation rate and D is the blowing snow divergence rate. All terms are expressed as mm of water equivalent per day ($\mathrm{mm\,w.e.\,day^{-1}}$).

In ERA-5, snow is regarded as an additional layer on top of the soil layer, and is characterized by a snow temperature T_{sn}, with independent and prognostic thermal and mass contents. Snow melting takes place if T_{sn} exceeds the melting point (273.16 K), while snow sublimation is estimated with the bulk aerodynamic formula using the wind speed and specific humidity of the lowest model layer and the saturated specific humidity at T_{sn} (ECMWF, 2016). The bulk aerodynamic formula, used in ERA-5, performed well in estimating the observed snow sublimation over the Himalayas (Stitger et al., 2018), but has not been evaluated over Antarctica. What is more, blowing snow is not accounted for in the reanalysis dataset, which is problematic as during Foehn events it is known to lower the albedo and increase surface compaction, and hence enhance the effects of Foehn on the snowpack (e.g. Bromwich, 1989; Scarchilli et al., 2010; MacDonald et al., 2018; Datta et al., 2019; Pradhananga and Pomeroy, 2022). As a result, the terms Q_{surf}, D and Q_{snow} in Eq. (2) are estimated as detailed below, while P and M are taken directly from the reanalysis. The ERA-5 predicted surface mass

anomaly, given by precipitation minus sublimation with the monthly mass accumulation over the period 1980-2001 removed, over the Dronning Maud Land in East Antarctica for 2006-2017 compares well with that estimated from the measurements collected by the Gravity Recovery and Climate Experiment satellite (Gossart et al., 2019). In fact, ERA-5 is the best performing reanalysis product out of those considered, closely following the satellite-derived estimates, with a mean absolute error of 24 Gt yr^{-1}. This justifies the use of the reanalysis' P and M in this work. All constants are defined in Table 1.

The surface sublimation rate, Q_{surf}, included in the term E in Eq. (2), is parameterized as

$$Q_{surf} = \rho' \frac{\rho_{air} \overline{(w'q')}}{\rho_{water}} = \rho' \frac{\rho_{air}(u_* q_*)}{\rho_{water}} \quad (3)$$

with

$$u_* = \frac{\kappa U}{ln\,ln\,\left(\frac{z + z_0}{z_0}\right)}$$

$$q_* = \frac{\kappa q_{si}(RH_{ice} - 1)}{ln\,ln\,\left(\frac{z + z_q}{z_q}\right)}$$

where u_* is the friction velocity, q_* is a humidity scale, κ is the von Karman constant, U is the wind speed at height z above the surface (taken to be 10-m), z_0 is the aerodynamic roughness length, q_{si} is the saturation mixing ratio over ice, RH_{ice} is the relative humidity with respect to ice, z_q is the roughness length for moisture over snow (taken to be the same as z_0), ρ is the air density, ρ_{water} is the density of water, and ρ' is a conversion factor from m s^{-1} to mm day^{-1}. If $RH_{ice} > 1$, q_* becomes positive and deposition to the surface is said to occur. The term $\overline{(w'q')}$ is the turbulent moisture flux at the surface, with $\rho_{air} \overline{(w'q')}$ giving the sublimation rate (van den Broeke, 1997). The rate of water equivalent lost to sublimation is obtained by dividing the sublimation rate by the density of water, as done by Montesi et al. (2004).

The blowing snow sublimation rate, Q_{snow}, is expressed as in Eq. (4) below

$$Q_{snow} = \frac{a_0 + a_1\xi + a_2\xi^2 + a_3\xi^3 + a_4 U_{10} + a_5\xi U_{10} + a_6\xi^2 U_{10} + a_7 U_{10}^2 + a_8\xi U_{10}^2 + a_9 U_{10}^3}{U'} \quad (4)$$

with

$$\xi = \frac{RH_{ice} - 1}{2\rho_{ice}[F_k(T) + F_d(T)]}$$

251
$$U' = \frac{\left(1 - \frac{U_t}{U_{10}}\right)^{2.59}}{\left(1 - \frac{6.975}{U_{10}}\right)^{2.59}}$$

252

253
$$U_t = 6.975 + 0.0033 \, (T_{2m} + 27.27)^2$$

254

255 where ξ is a thermodynamic term, U_{10} is the 10-m wind speed, U' is a non-dimensional factor that
256 removes the dependence on the saltation mixing ratio, U_t is the threshold for initiation of blowing
257 snow, T_{2m} is the 2-m temperature, ρ_{ice} is the density of ice, and $F_k(T)$ and $F_d(T)$ are the
258 conductivity and diffusion terms associated with sublimation, both temperature dependent and
259 extracted from Rogers and Yau (1989). While negative values of Q_{surf} indicate sublimation and
260 positive values denote deposition, the opposite is true for Q_{snow}, with positive values implying
261 sublimation of blowing snow is taking place.

262

263 The snow transport rate, Q_t, is a vector quantity whose magnitude is given by

264
$$Q_t = BU_{10}^C \quad (5)$$

265 with the direction obtained by projecting it onto the 10-m horizontal wind vector. The divergence
266 term D in Eq. (2) is then obtained by

267
$$D = \frac{\rho'}{\rho_{water}} \nabla \cdot Q_t \quad (6)$$

268

Constant	Value	Constant	Value
a_0	3.78407×10^{-1}	a_8	1.56862×10^{-3}
a_1	-8.64089×10^{-2}	a_9	-2.93002×10^{-4}
a_2	-1.60570×10^{-2}	κ	0.4
a_3	7.25516×10^{-4}	ρ'	8.6400×10^7
a_4	-1.25650×10^{-1}	ρ_{water}	$1000 \ \mathrm{kg\,m^{-3}}$
a_5	2.48430×10^{-2}	ρ_{ice}	$917 \ \mathrm{kg\,m^{-3}}$
a_6	-9.56871×10^{-4}	B	$2.2 \times 10^{-6} \ \mathrm{kg\,m^{-5.04}\,s^{3.04}}$
a_7	1.24600×10^{-2}	C	4.04

269

270   **Table 1:** Constants used in the surface mass balance.

271

3. Foehn Events at PIG and Impacts on Ice

273   The statistics of Foehn events at PIG are summarized in Fig. 2. Foehn is more frequent in the
274 austral winter season, in particular from June to October, and less common in the summer albeit
275 with a considerable spread in all months (Fig. 2a). The annual cycle in the duration of Foehn events
276 is less pronounced, with monthly-mean values in the range 5 to 9 h, with August featuring both the
277 highest number (~123) and longest (~9 h) Foehn episodes. At the Antarctic Peninsula, Foehn
278 occurrence peaks in the transition seasons (Wiesenekker et al., 2018; Laffin et al., 2021) whereas
279 at the McMurdo Dry Valleys located next to the Ross Sea it is more frequent in winter (Speirs et
280 al., 2013). As Foehn events are driven by large-scale pressure gradients, the difference in the
281 timing of the peaks is likely a result of the variability in the position of the baroclinic systems. In
282 particular, and as noted by Simmonds et al. (2003), the cyclonic activity in the Ross Sea, northern
283 Antarctic Peninsula and around PIG is maximized in winter whereas in the central Antarctic
284 Peninsula it is the highest in the summer. Consistent with this, in the Amundsen and
285 Bellingshausen Seas there is a pronounced equatorward shift in the mid-latitude storm track in the
286 summer months (Dias da Silva et al., 2021), which is in line with the higher occurrence of Foehn
287 at PIG in the colder months. The Amundsen Sea Low (ASL), a semi-permanent low pressure in
288 the Amundsen-Bellingshausen Seas (60º-75ºS and 170º-290ºE) that exhibits the largest
289 geopotential height variability in the Southern Hemisphere, is likely to play a major role in the
290 occurrence of Foehn at PIG (Mclennan and Lenaerts, 2021). Meridionally, it is at its most poleward
291 location in late winter and is shifted further equatorwards in the summer, while longitudinally it is
292 the closest to PIG in the summer months (Raphael et al., 2016). As Foehn is more likely when the
293 ASL is just to north of PIG with its clockwise circulation encouraging Foehn effects in the region,
294 as noted in section 4, the intricate annual cycle of the ASL may explain the highest Foehn
295 occurrence in late winter and why it still takes place in the summer months. In the area around
296 PIG, there are on average 3.0 Foehn days in the month of August (123 occurrences over the 41-
297 year period 1980-2020) lasting roughly 7.9 h each, whereas in January there are 0.37 Foehn days
298 per month that typically last for about 5.1 h. Wiesenekker et al. (2018) reported an average of 1.3
299 to 5.8 Foehn events per month in the Antarctic Peninsula over 1979-2016, with roughly 70-80%
300 of the events in December 2014 - December 2016 lasting less than a day. These figures are higher
301 than those at PIG shown in Fig. 2a, which is due to the fact that the Antarctic Peninsula is more
302 exposed to the mid-latitude storm track, with the higher terrain on its western side promoting Foehn
303 effects.

304

305 Fig. 2b gives the area-averaged air temperature and sensible heat flux for the Foehn events, with
306 the air temperature, sensible heat flux and RH anomalies during Foehn episodes plotted in Fig. 2c.
307 The sensible heat flux is positive, and hence directed downwards towards the surface, with
308 monthly-mean values in the range 18 to 42 W m^{-2}, with higher values in the winter months. This is

in line with Laffin et al. (2021) and with the fact that the sensible heat flux around Antarctica is maximized in the colder months when the surface to air temperature gradient is the highest, owing to the sharp thermal inversions that develop at this time of the year (Reijmer et al., 1999). The magnitude of the fluxes is comparable to that modeled over the Antarctica Peninsula (e.g. Elvidge et al., 2014) and at Joyce Glacier in McMurdo Dry Valleys (Hofsteenge et al., 2022). The air temperature during Foehn events at PIG is below freezing, ranging from -7ºC in January to -22ºC in August. However, melting and sublimation can still occur, in particular when accounting for the large variability which is maximized in the summer (e.g., Ghiz et al. 2021). Fig. 2c shows that Foehn effects lead to generally warmer (air temperatures anomalies typically of +0-7ºC) and drier (RH anomalies in the range -8% to -11%) weather conditions accompanied with a downward sensible heat flux (anomalies of +14-21 W m^{-2}).

Fig. 2d gives the trends in the number of Foehn days and in the duration of Foehn events for 1980-2020, both of which are not statistically significant. When the analysis is extended to individual seasons, only one statistically significant trend is found, that of the duration for the autumn season, with a slope of about -0.002 days yr^{-1} (not shown). Studies of trends of Foehn occurrence in Antarctica also reported non statistically significant slopes, in particular over the two major studied regions of the McMurdo Dry Valleys (e.g., Speirs et al., 2013) and the Antarctic Peninsula (e.g., Laffin et al., 2021). Fig. 2d also shows considerable inter-annual variability in both the number and duration of Foehn days. The major peaks taking place mostly in La Nina (1984, 1985, 1999, 2010) or neutral (1981, 1993, 1996, 1999, 2003, 2008, 2013) years, while the minimum in 1982, 1986, 1997 and 2015 coincide with El Nino years (Lestari and Koh, 2016; Zhang et al., 2022). In La Nina conditions, the ASL is more active than normal (Raphael et al., 2016), which may promote the occurrence of Foehn, while in El Nino episodes the presence of a ridge over the Amundsen and Bellingshausen Seas (Yuan, 2004) may discourage Foehn effects at PIG. A discussion of the large-scale patterns that favor Foehn occurrence at PIG is given in section 4.

(a)   (b)
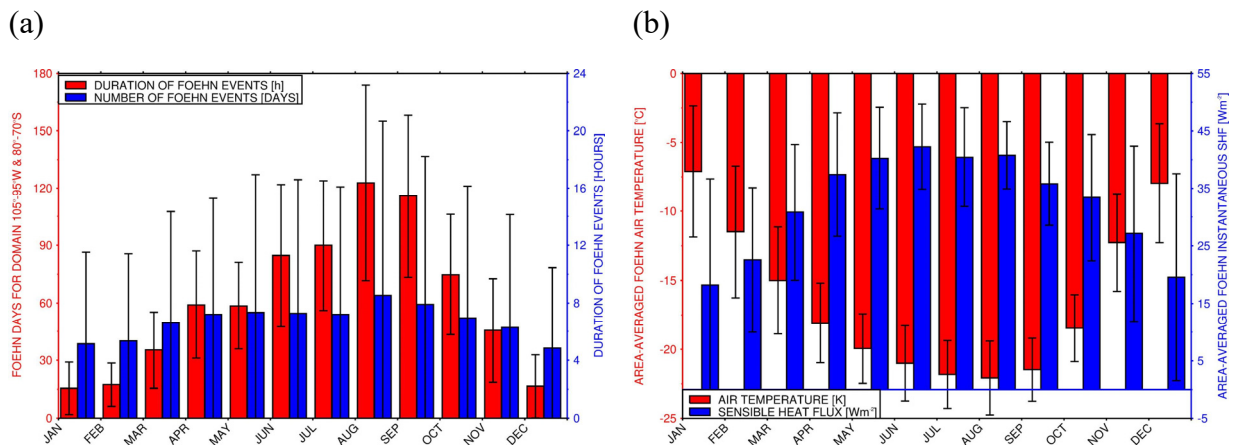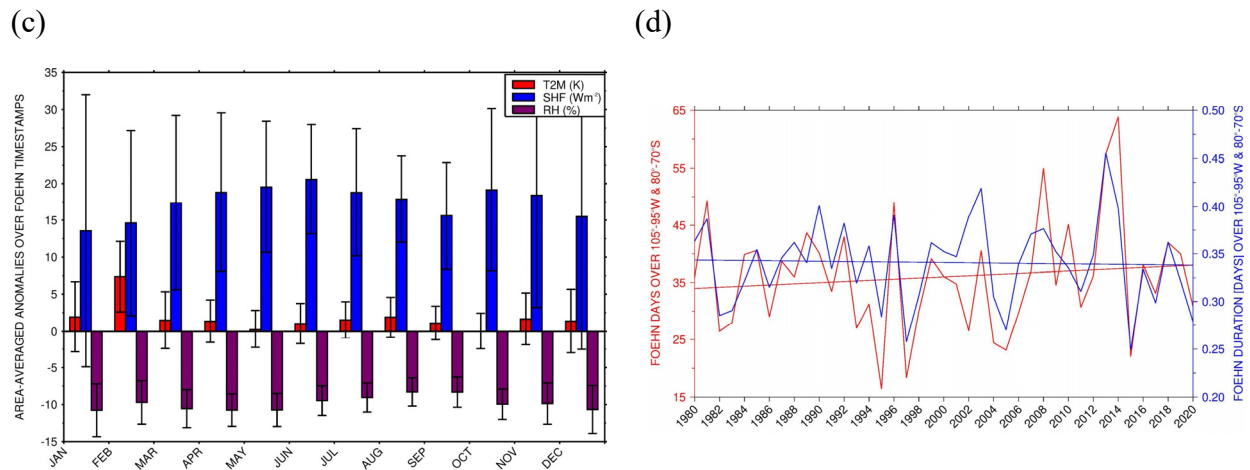
Figure 2: **Climatology and trends of Foehn events:** (a) Monthly mean (histogram bars) and standard deviation (error bars) of Foehn days (orange; left axis) and duration of Foehn events (hours; blue; right axis) for the period 1980-2020 and for the domain 95ºW-105ºW and 80ºS-70ºS. (b) is as (a) but for the area-averaged air temperature (ºC; orange; left axis) and instantaneous sensible heat flux (W m^{-2}; blue; right axis; positive if downwards towards the surface). (c) gives the air temperature (ºC; orange), instantaneous sensible heat flux (W m^{-2}; blue) and relative humidity (%; purple) anomalies during Foehn timestamps. (d) Trend in Foehn days (left; red) and in the duration of Foehn events (right; blue) for 1980-2020. The slopes of the Foehn days and duration are 0.101024 days yr^{-1} and -0.0001 days yr^{-1} with a statistical significance of 55% and 18%, respectively.

337

338   A quantification of the potential for surface melting and sublimation is presented in Fig. 3. The
339   "melt potential" index (MPI) is defined following Orr et al. (2022) using the daily maximum air
340   temperature for 1980-2020, for both the full year and extended summer season (November to
341   February, NDJF). At each grid-point, the MPI intensity is given by the difference between the 95th
342   percentile of the daily maximum air temperature distribution for the Foehn/no-Foehn days and the
343   melt threshold of 273.15 K, while the MPI frequency is the percentage of values higher than the
344   threshold. The "sublimation potential" index (SPI) is defined in the same way but using the 95th
345   percentile of the daily maximum of the hourly surface sublimation given by Eq. (3) and a threshold
346   of zero, while its frequency expresses the percentage of the Foehn/no-Foehn days in the 1980-
347   2020 period when there is sublimation for at least one hour per day at the site. Here, the difference
348   between Foehn and no-Foehn timestamps is plotted for both indices to give insight into the effects
349   of Foehn in surface melting and sublimation.

350

351   Surface melting is less common at PIG during Foehn events, with a MPI intensity and frequency
352   reductions of about -1.3 K and -3%, respectively, with comparable values in NDJF (-0.9 K and -
353   6%). This is expected, as the downward sensible heat flux is largely offset by the upward latent
354   heat flux that arises from the drier near-surface air, making it harder for the snowpack to melt.
355   Surface melting is confined to lower elevations where the temperature is higher. Here, there is also
356   increasing exposure to the warmer and more moist maritime air masses compared to the high
357   terrain inland. The fact that surface melting is more frequent in the adjacent Southern Ocean in
358   Foehn episodes may be attributed both to the increased adiabatic compression of the winds as they

359 descend towards the coastal regions, and the likely presence of a low pressure system north of the
360 site during the Foehn events, as will be discussed in section 4. When all days (Foehn and no-
361 Foehn) in 1980-2020 are considered, the MPI intensity and frequency at PIG for the full year are
362 -0.27 K and 4%, respectively, and +0.87 K and 10% for NDJF (not shown). Orr et al. (2022) used
363 higher spatial resolution (~12 km) modelling products over December-February 1979-2019 and
364 for the whole Antarctica, to obtain values at PIG of 1.3-1.7 K and 23.7-23.8%. The MPI intensity
365 and frequency difference between Foehn and no-Foehn days given in Figs. 3a-b stress the role of
366 Foehn in discouraging surface melting at and around the glacier. Figs. 3c-d are as Figs. 3a-b but
367 for the SPI. The seasonal variability is much reduced compared to that of the MPI, with an intensity
368 difference between Foehn and no-Foehn days of +1.8 mm w.e. day^{-1} for the full year and +1.6 mm
369 w.e. day^{-1} for NDJF, and a rather small change in frequency (<0.3%). When all days are taken, the
370 intensity magnitudes are of about 3.34 and 3.39 mm w.e. day^{-1}, respectively, and a frequency of
371 occurrence around 100% (not shown). The fact that the frequency is very high indicates that the
372 daily maximum in the surface sublimation is positive nearly all the time at PIG, suggesting that
373 there is at least 1 h of sublimation every day of the year for the 41-year period at the site. This also
374 explains why there is hardly any change in frequency between Foehn and no-Foehn days. The SPI
375 intensity, on the other hand, is roughly 50% larger during Fohn episodes, highlighting the role of
376 Foehn effects in the surface sublimation. It is interesting to note that, even though the near-surface
377 wind in the region is stronger in the colder months, the effects of Foehn on the 10-m wind in NDJF
378 are largely similar to that in the full year (cf. Figs. 3c-d). The convergence of the near-surface wind
379 in the PIG basin and the lower heights and consequently higher temperatures explain the maximum
380 in surface sublimation in the region seen in Figs. 3c-d.
381
382   In order to explore the contribution of Foehn to the surface mass balance, Figs. 4a-f show the
383 composite difference of the terms in Eq. (2) between Foehn and no-Foehn timestamps for 1980-
384 2020. The Foehn minus no-Foehn values of the rate of accumulation or storage of snow at the
385 surface (S), precipitation (snowfall) rate (P), surface melt and runoff rate (M), surface sublimation
386 rate (Q_{surf}), blowing snow sublimation rate (Q_{snow}) and blowing snow divergence rate (D) at
387 PIG are $S \sim$ -1.411, $P \sim$ -0.345, $M \sim$ -0.005, $Q_{surf} \sim$ -1.434, $Q_{snow} \sim 0$ and $D \sim$ -0.363 mm w.e.
388 day^{-1}, respectively. This indicates that (i) surface sublimation plays the dominant role in the surface
389 mass balance during Foehn events (note that negative values of the surface sublimation rate, Q_{surf},
390 and positive values of the blowing snow sublimation rate, Q_{snow}, indicate sublimation); (ii) the
391 sum of the two blowing snow terms, Q_{snow} and D, has a magnitude comparable to that of the
392 precipitation/snowfall, P, roughly 25% smaller than that of the surface evaporation, but with the
393 opposite sign in Eq. (2), reflecting a lack of snowfall during Foehn episodes due to the drier
394 conditions while the convergence of blowing snow at the glacier basin adds to the surface mass;
395 (iii) snow melting, M, makes a negligible contribution to the surface mass balance, being roughly
396 three orders of magnitude smaller than the surface sublimation.
397

398   The surface sublimation rate (Fig. 4c) is considerable, with the values at PIG comparable to the
399   maximum rates at a site in northern Victoria Land during November 2018 (Ponti et al., 2021),
400   but roughly an order of magnitude smaller than that due to melting resulting from ice dynamics
401   around Antarctica, including at PIG (Holland et al., 2007; Rintoul et al., 2016; Feldmann et al.,
402   2019). Surface melting is negligible and confined to the coastal regions further north (Fig. 4d). As
403   noted by Scarchilli et al. (2010), and in line with our findings (Figs. 4e-f), blowing snow plays an
404   important role in the surface mass balance during strong wind (here Foehn) episodes. The
405   magnitude of the total blowing snow sublimation and transport reported in that study, which are
406   measured at the Terra Nova Bay in the Ross Sea, are larger than those estimated here at PIG. This
407   is consistent with the fact that katabatic wind events at Terra Nova Bay can be quite strong, being
408   associated with much higher wind speeds than those during the Foehn events discussed here
409   (Aulicino et al., 2018). Blowing snow sublimation (Fig. 4e) peaks just south and east of the glacier,
410   with values in the range 0.5-0.75 mm w.e. day^{-1}, where the wind speed exceeds the threshold for
411   blowing snow sublimation, Eq. (4). The convergence of the blowing snow transport rate from the
412   east and southeast of PIG leads to the negative divergence at the basin (Fig. 4f). The negative
413   values in the snowfall rate plot to the south and north of PIG, Fig. 4b, reflect the reduced
414   precipitation in association with Foehn events. The changes in the storage term between Foehn
415   and no-Foehn timestamps, Fig. 4a, are comparable to the modelled surface mass balance in the
416   region (Donat-Magnin et al., 2021), suggesting that Foehn events are a major contributor to it.
417   Figs. 4g-h gives the differences in the 10-m wind speed and sensible heat flux. During Foehn
418   episodes, there is a strengthening of the near-surface wind by 5-10 m s^{-1} with it converging into
419   PIG. The sensible heat flux increases by about 30-40 W m^{-2}, in line with the area-averaged values
420   in Fig. 2b. While in other regions of Antarctica, such as the Antarctica Peninsula, Foehn plays an
421   active role in snow melting (Laffin et al., 2021), at PIG it seems to trigger mostly sublimation.
422

   (a)
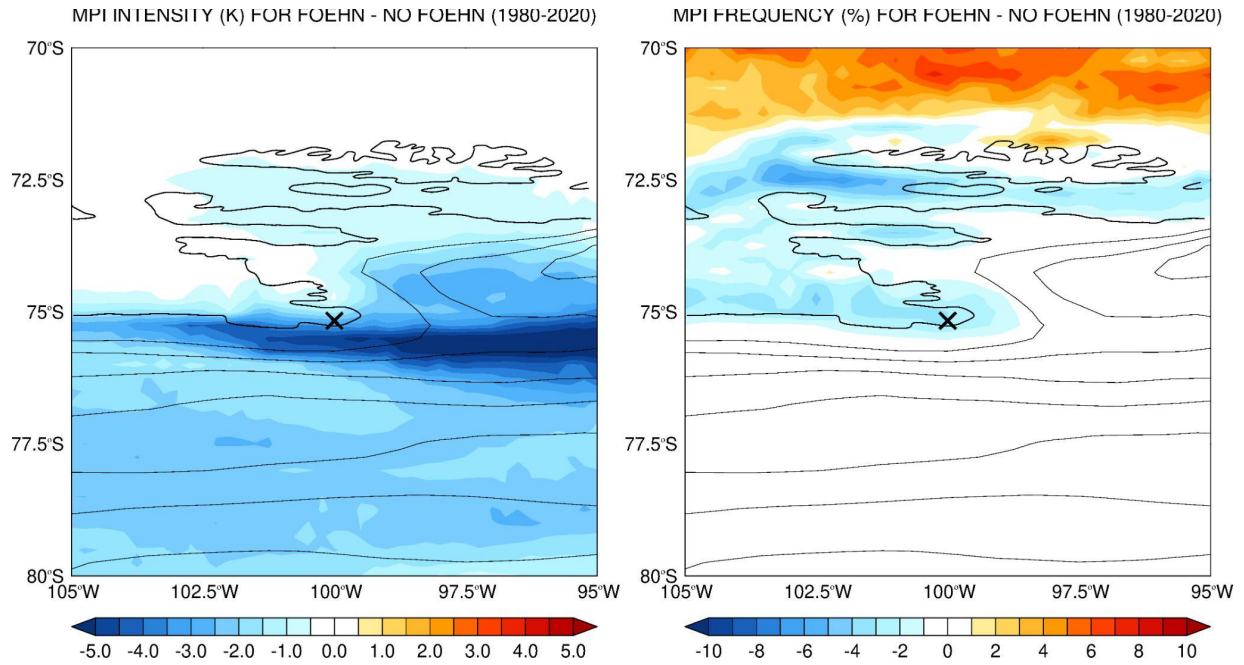
(b)
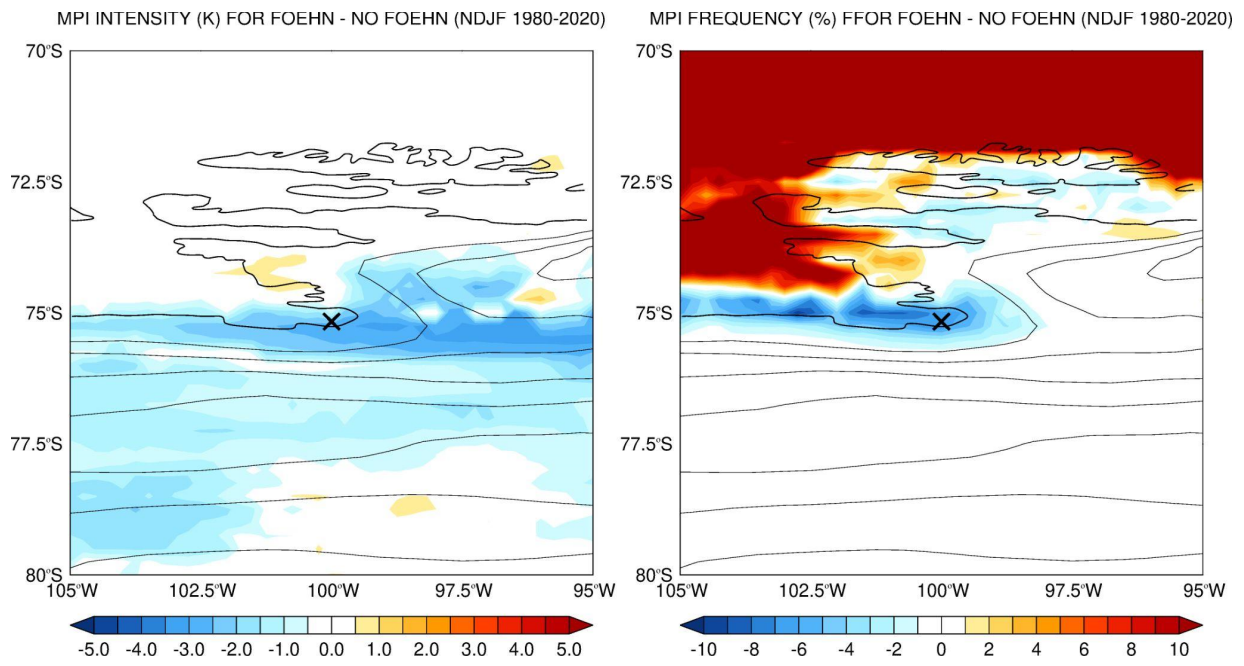
(c)
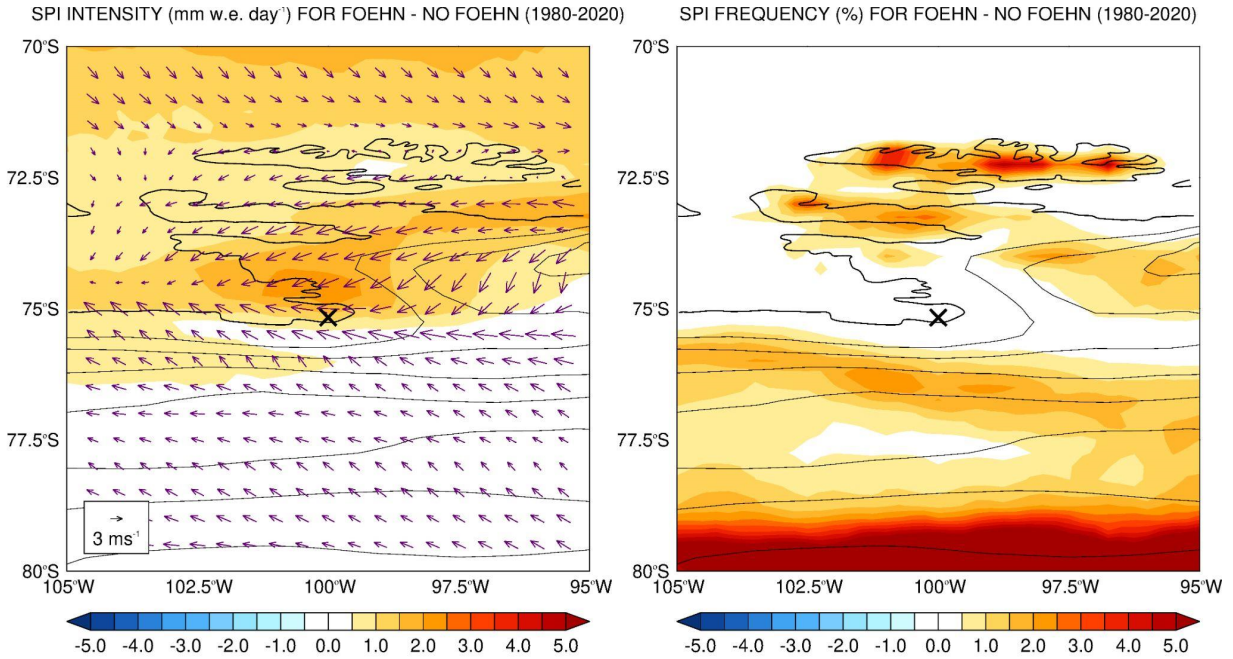
(d)
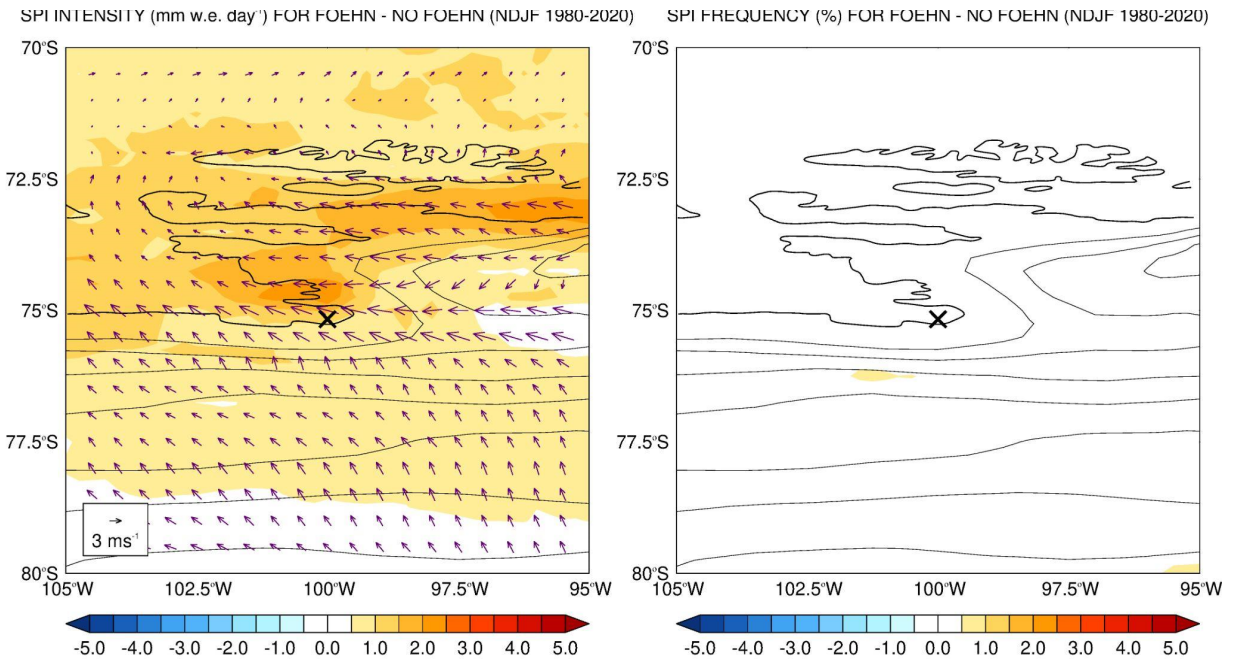
Figure 3: **Melt and Sublimation Potential Indices:** (a) "Melt Potential" index (MPI) intensity (K; left) and frequency (%; right), defined following Orr et al. (2022), for the difference between Foehn and no-Foehn timestamps for 1980-2020. The thin black lines are 250 m orography contours and the land-sea mask is represented by the thick black line. The cross gives PIG location (100ºW, 75º10'S). (b) is as (a) but for November-February (NDJF) only. (c)-(d) are as (a)-(b) but for the "Sublimation Potential" index (SPI), with the intensity given in mm of water equivalent per day (mm w.e. day⁻¹). The averaged 10-m horizontal wind vectors are drawn as arrows in the left panels of (c)-(d) for the respective period.
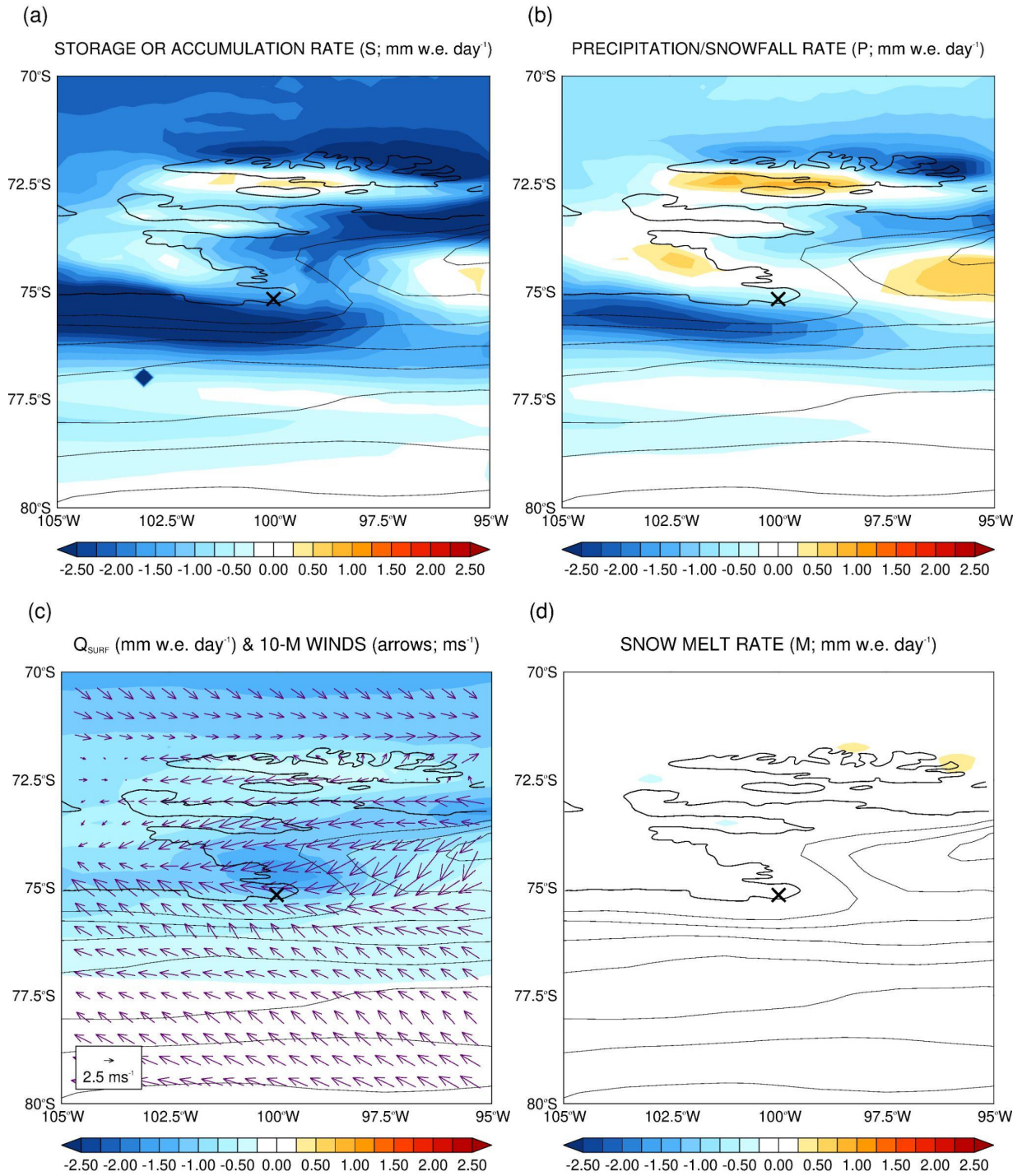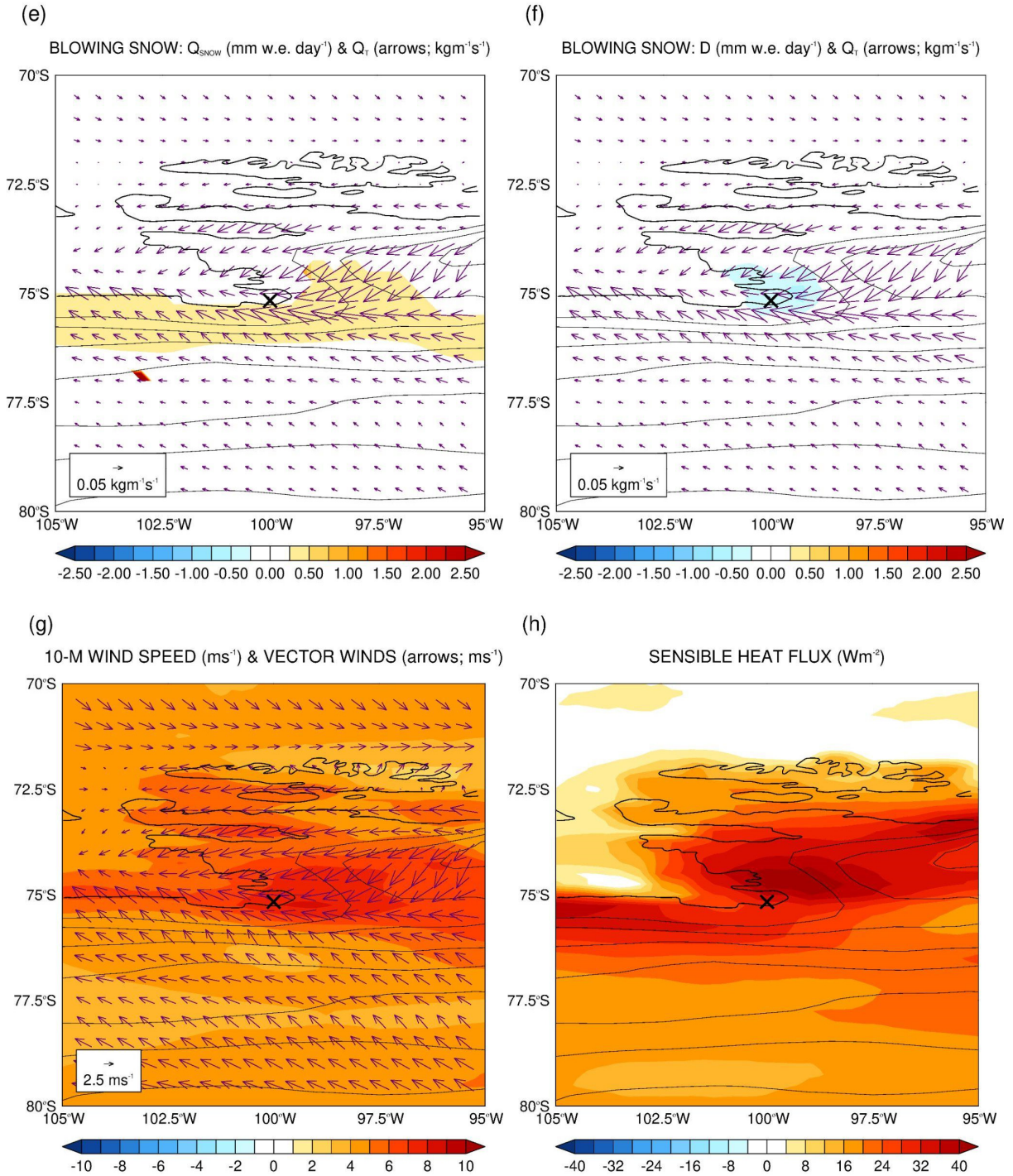
Figure 4: Composite difference between Foehn and no-Foehn timestamps for 1980-2020: (a) Storage or accumulation rate of snow at the surface (S in Eq. (2); mm w.e. day^{-1}), (b) precipitation/snowfall rate (P; mm w.e. day^{-1}), (c) surface sublimation rate (Q_{surf}; mm w.e. day^{-1}; positive values indicate deposition to the surface and negative values indicate sublimation), (d) snow melt rate (M; mm w.e. day^{-1}; positive values indicate melting), blowing snow (e) sublimation rate (Q_{snow}; mm w.e. day^{-1}; positive values indicate sublimation) and (f) divergence rate (D; mm w.e. day^{-1}), (g) 10-m wind speed (shading; m s^{-1}) and (h) instantaneous surface sensible heat flux (W m^{-2}, positive if downwards towards the surface). The arrows in (c) and (g) give the 10-m horizontal wind vectors (m s^{-1}) while in (e)-(f) they show the blowing snow transport rate (Q_t; kg m^{-1} s^{-1}).

4. Large-scale Circulation Favorable for Foehn Occurrence

Foehn events are driven by large-scale pressure gradients, so it is of interest to investigate the patterns in the atmospheric circulation which promote their occurrence around PIG. The k-means clustering technique (Steinley, 2006) is applied to the daily 200 hPa and 850 hPa geopotential height and wind anomalies and to the sea-level pressure and 10-m wind anomalies for the Foehn days identified in 2000-2020. However, and to exclude localized events, only days when Foehn occurred in at least 10% of the 105º-95ºW and 70º-80ºS region are considered, leaving 1181 days for the analysis. A different number of clusters from one to five are tested, and the optimal number, as determined by a silhouette analysis (Rousseeux, 1987), is found to be two (not shown). Cluster 1 (Figs. 5a-b), which features the negative phase of the Antarctic Oscillation (AAO; Gong and Wang, 1999), accounts for ~58% of the total Foehn events. Cluster 2 (Figs. 5c-d), which projects onto the positive phase of the Southern Annular Mode (SAM; Marshall et al., 2003), an index which gives an indication of the strength and latitudinal position of the westerlies in the Southern Hemisphere, accounts for ~42% of the 1181 Foehn episodes. The clusters' annual cycle is given in Fig. 5e. For computational reasons the cluster analysis was not extended to 1980-2020. In any case, the findings are unlikely to change should the technique be applied to the 41-year period, with the AAO and SAM most certainly the dominant modes.

The first cluster (Fig. 5a) comprises a wavenumber #1 with an equatorward shift in the mid-latitude storm track as evidenced by the high pressure over Antarctica and a nearly circumglobal low pressure equatorwards. It corresponds to the negative phase of the AAO, with the easterly to northeasterly winds around PIG promoting the occurrence of Foehn. The air mass comes from the Weddell sector and moves over the Ellsworth Land before flowing down the length of PIG drainage basin (Fig. 5b). The wavenumber #1 is maintained by both low-latitude forcing (Quintanar and Mechoso 1995a and b) and the high topography of Antarctica (Hoskins and Karoly, 1981). As noted by Pohl et al. (2010), the AAO has a strong correlation with ENSO, with El Nino events favoring its negative phase. This mode dominates in the colder months from May to August (Fig. 5e) when the ASL is displaced westwards (Raphael et al., 2016) and hence the SAM has a smaller impact on the weather conditions at PIG.

The second cluster (Fig. 5c) projects onto the positive phase of the SAM in which the storm track is shifted poleward and the ASL is significantly deeper (Fogt and Marshall, 2020; Zheng and Li, 2022). Mclennan and Lenaerts (2021) found that the ASL modulates the total annual snowfall at the Thwaites Glacier adjacent to PIG (Fig. 1a). This cluster shows the winds descending the slopes immediately to the east of the Pine Island ice shelf. The air mass comes from the Pacific Ocean and flows over the high terrain and coastal mountains directly to the northeast of PIG before descending downslope into the glacier basin (Fig. 5d). The cyclonic (clockwise) circulation motion associated with the ASL, and its interaction with the high terrain to the east of PIG, leads to Foehn conditions around the glacier. Cluster #2 features a wavenumber #3 across the Southern Hemisphere.

(a) 200hPa Z [m] & WIND [ms⁻¹] ANOMALIES FOR CLUSTER #1

(b) MSLP [hPa] & 10-M WIND [ms⁻¹] ANOMALIES FOR CLUSTER #1

(c) 200hPa Z [m] & WIND [ms⁻¹] ANOMALIES FOR CLUSTER #2

(d) MSLP [hPa] & 10-M WIND [ms⁻¹] ANOMALIES FOR CLUSTER #2
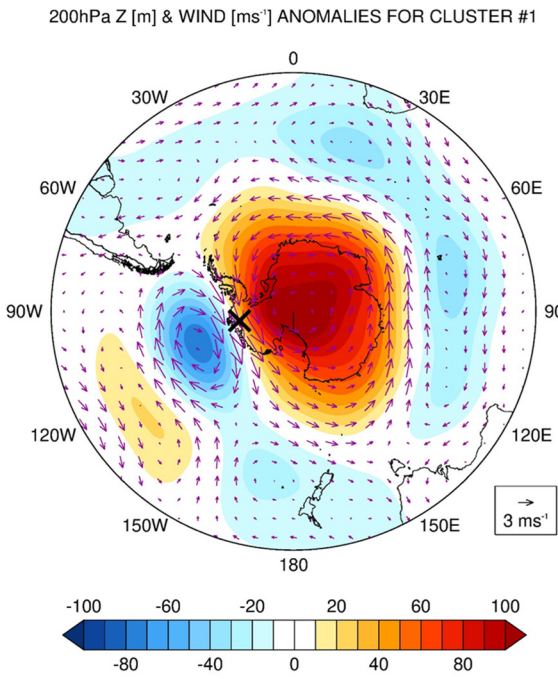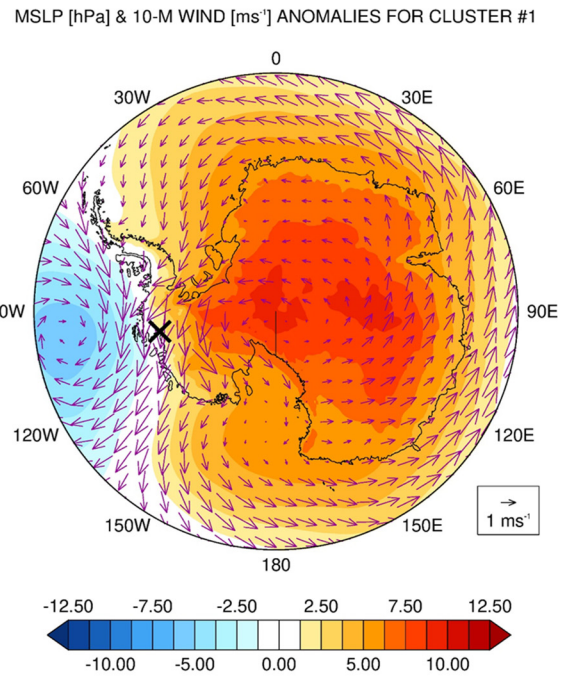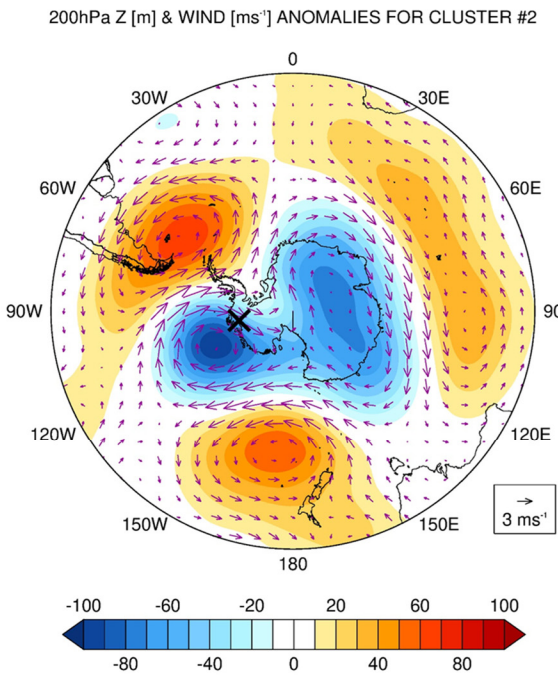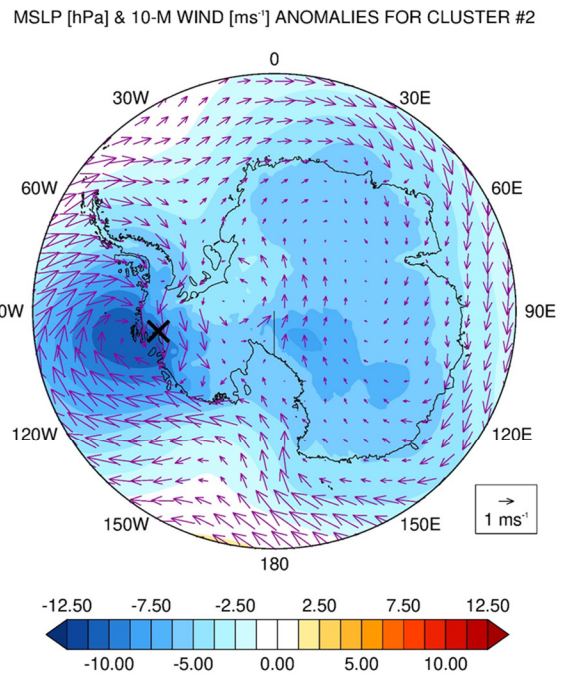
(e)
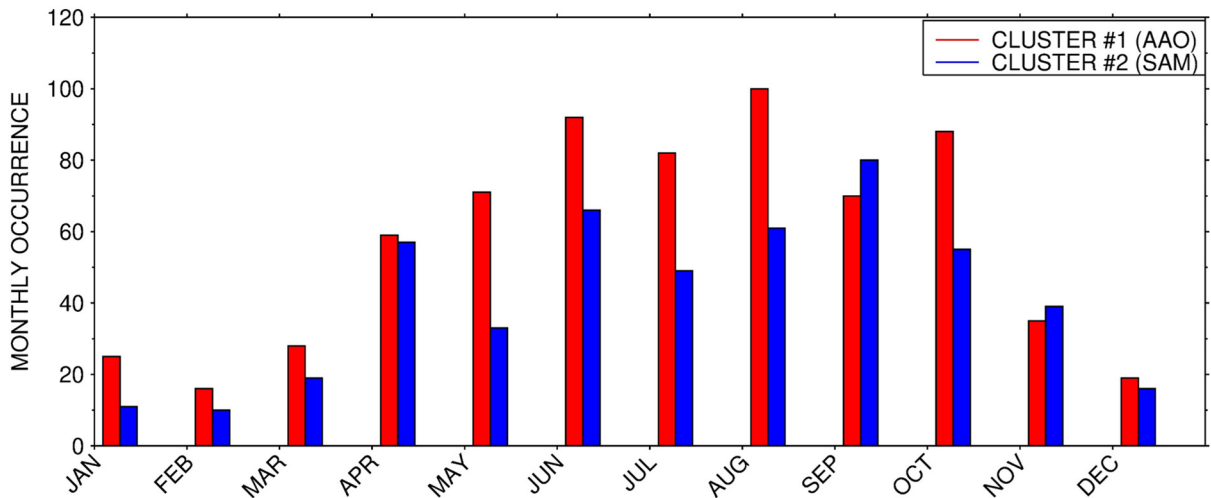
Figure 5: **Large-scale conditions promoting Foehn events:** (a) 200 hPa geopotential height anomalies (shading; m) and wind vectors (arrows; m s^{-1}) and (b) mean sea-level pressure (shading; hPa) and 10-m wind vectors (arrows; m s^{-1}) for cluster #1 of a k-means clustering technique applied to the daily-mean fields of 1181 Foehn days at PIG in 2000-2020. The cross gives the approximate location of PIG (100ºW, 75º10'S). (c)-(d) are as (a)-(b) but for cluster #2. The monthly occurrence of each cluster is given in panel (e).

5. Illustrative Case Study: November 2011

464

465   The effects of Foehn at PIG are discussed for an event in November 2011. Fig. 6 summarises
466   the large-scale environment that promoted the occurrence of Foehn, while Fig. 7 presents a time-
467   series of spatially-averaged meteorological variables that allows for a quantification of the Foehn
468   effects.
469

470   The ASL was particularly deep on 10-11 November 2011, with the 500 hPa geopotential height
471   anomalies more than 1.5 ⌠ below the 1979-2020 mean (Figs.6a-b). An atmospheric river associated
472   with an elongated and narrow band of high moisture content and integrated vapour transport (IVT)
473   values in the top 10% of the climatological distribution, extended from the Southern Hemisphere
474   mid-latitudes into West Antarctica and PIG, being transported by the clockwise circulation of the
475   ASL. As the ASL edged closer to the Antarctica Peninsula on 11 November (Fig. 6b), the more
476   moist air, now over the Weddell Sea, penetrated further inland reaching PIG and the surrounding
477   region from the east (after flowing over the ice divide that separates the Weddell Sea and Ronne
478   Ice Shelf from PIG and the Amundsen Sea region). As a result, the IVT at PIG more than doubled
479   from about 27.5 kg m^{-1} s^{-1} on 10 November to around 65 kg m^{-1} s^{-1} on 11 November, with the total
480   column water vapour increasing to just under 4 kg m^{-2} (Fig. 7a). The Foehn effect in this event
481   corresponds to that of cluster #1 (Fig. 4a), the more indirect pathway from the Weddell Sea as
482   opposed to Foehn events triggered by Pacific warm air intrusions (cluster #2, Fig. 4b).
483

484 As seen in Figs. 6c-d, the air mass accelerated downslope as it descended the mountains towards
485 coastal West Antarctica, with 10-m wind speeds higher than $20\,\mathrm{m\,s^{-1}}$ and in the top 10% of the
486 climatological distribution over a vast region including PIG (locally in the top 1% just to the
487 northwest and southeast of PIG), and downward sensible heat fluxes in excess of $75\,\mathrm{W\,m^{-2}}$ at PIG
488 (the negative, or upward pointing, fluxes around 75ºS and 110ºW are associated with a sea ice-
489 free area). These tendencies are seen in the area-averaged time-series (Fig. 7c) with the negative
490 (upward) latent heat flux indicating sublimation peaking on 11 November (Fig. 7f). In fact, the
491 phase of the latent heat flux matches that of the surface sublimation given in Fig. 7f. The opposite
492 sign of the sensible and latent heat fluxes, which roughly offset each other, is expected during
493 Foehn events (Elvidge et al., 2020), as the positive latent heat flux which arises due to sublimation
494 is opposed by the downward sensible heat flux due to the higher air than surface temperature. The
495 surface mass balance is essentially controlled by the surface and blowing snow sublimation, with
496 the precipitation/snowfall and the divergence terms playing a secondary role, and with the snow
497 melting being zero throughout the full period (Fig. 7f). The estimated maximum sublimation rate
498 is seen at the end of 10 November and has a magnitude of $\sim 0.13\,\mathrm{mm\,w.e.\,hr^{-1}}$, comparable to the
499 ice loss due to ocean dynamics (e.g., Holland et al., 2007; Rintoul et al., 2016; Feldmann et al.,
500 2019) albeit in a non-sustained way. The ERA-5 snow depth, which accounts only for sublimation
501 and changes in snow density (snow melt is not simulated by ERA-5 during this event, Fig. 7f),
502 shows a steady decrease starting on 04 November and a faster drop from 11-13 November (not
503 shown). The reanalysis snow depth during this period is around $9.21\,\mathrm{m\,w.e.}$, within the range of
504 that observed during field campaigns discussed in Konrad et al. (2019). Besides sublimation,
505 melting was detected in the Moderate Resolution Imaging Spectroradiometer (MODIS; Kaufman
506 et al., 1997) satellite imagery reaching a maximum on 12 November (Fig. 7g). The melting area at
507 times exceeded $\sim 100\,\mathrm{km^2}$ or roughly 2% of the central trunk of the glacier (Wingham et al., 2009).
508 The fact that ERA-5 does not simulate the observed melting can be attributed to the way snow
509 melting is parameterized in the model used to generate the reanalysis dataset, only taking place if
510 the temperature of the snow layer exceeds the melting point (ECMWF, 2016), with ERA-5
511 exhibiting a cold bias over the high terrain in Antarctica (e.g. Gonzalez et al., 2021). The observed
512 melting area is also much smaller than ERA-5's spatial resolution (~ 27 km $\times$ 27 km). Further
513 insight into the surface melt can be gained by running a surface balance model at high spatial
514 resolution that can be driven by ERA-5 data. This will be left for future work.
515
516 In Figs. 7d-e, the net shortwave, longwave and radiation fluxes from the reanalysis data are
517 compared with those estimated from satellite data, as given by the Clouds and Earth's Radiant
518 Energy System (CERES) SYN1deg dataset (Doelling et al. 2013, 2016). ERA-5 under-predicts
519 the net shortwave radiation flux during the day by up to a factor of 2.5, and the net longwave
520 radiation flux at night by up to $25\,\mathrm{W\,m^{-2}}$. These differences are consistent with those reported by
521 Ghiz et al. (2021), who attributed the lower shortwave fluxes in ERA-5 compared to CERES to
522 differences in the cloud properties, with the reanalysis fluxes being more consistent with those
523 measured in situ at a site in the West Antarctic Ice Sheet than those of CERES. On the other hand,

524 CERES partially corrects the tendency of ERA-5 to under-predict the net longwave radiation flux
525 over Antarctica, in particular in clear-sky conditions (Silbert et al., 2019). During the November
526 Foehn event, the area-averaged surface energy flux, F_{net}, is positive (Fig. 7e), as the positive
527 sensible heat flux offsets the negative latent heat flux (Fig. 7c), and the surface net shortwave
528 radiation flux overwhelms the negative net longwave flux (Fig. 7d). This indicates an excess of
529 energy towards the surface leading to snow melt and evaporation. The 3-5ºC increase in air
530 temperature (Fig. 7b) with respect to the previous non-Foehn days, present both in the reanalysis
531 and weather station data, is comparable to that seen during a Foehn event at the Ross Ice Shelf in
532 January 2016 (Zou et al., 2019). Note that the ERA-5 values are area-averaged over the red box in
533 Fig. 1a and hence the fields are likely larger in local areas.
534
535   The Foehn event can also be seen in the Hovmoeller plots in Fig. 6e. The wind direction shifts
536 from northeast to southeast on 08-09 November 2011 around PIG as the ASL moves closer to the
537 Antarctica Peninsula. This is accompanied by an increase in the sensible heat flux, with a
538 latitudinally-averaged value exceeding 50 W m^{-2} that corresponds to an anomaly of about 40 W m^{-}
539 ^{2}. The fact that the peak in wind speed takes place ~90ºW but that in the heat fluxes around 100º-
540 110ºW is consistent with the warming of the air mass as it descends the slopes of the mountains
541 over West Antarctica. The drying of the atmosphere in association with the Foehn effects is also
542 present, with the RH dropping below 70% during the event. The sensible heat flux shows a clear
543 diurnal cycle, peaking around 05-06 UTC, which is roughly 00 Local Time (LT) for a longitude of
544 ~100ºW, out-of-phase with the surface radiation fluxes (Figs. 7c-e). This mismatch is also seen on
545 other days, and may be attributed to the effects of Foehn, clouds and moisture on the heat fluxes.
546 Weaker Foehn events, with peak wind speeds roughly half of that on 09-11 November but similar
547 values of RH, took place earlier in the month, on 03-04 November 2011.
548
549

(a)   (b)
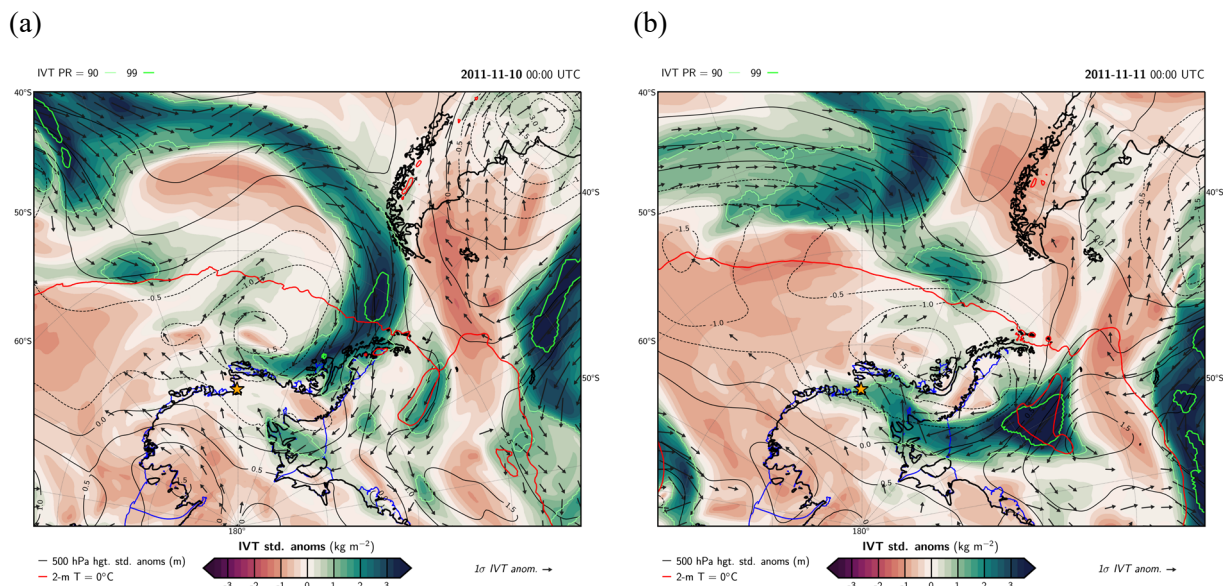
(c)
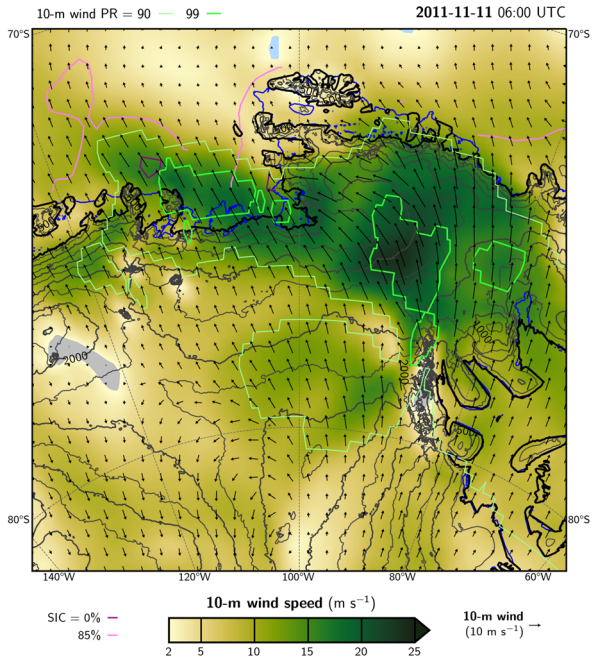
(d)
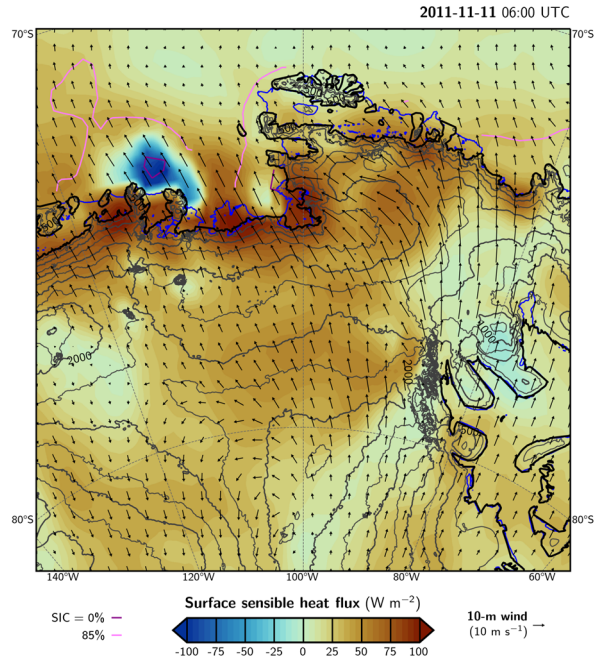
(e)
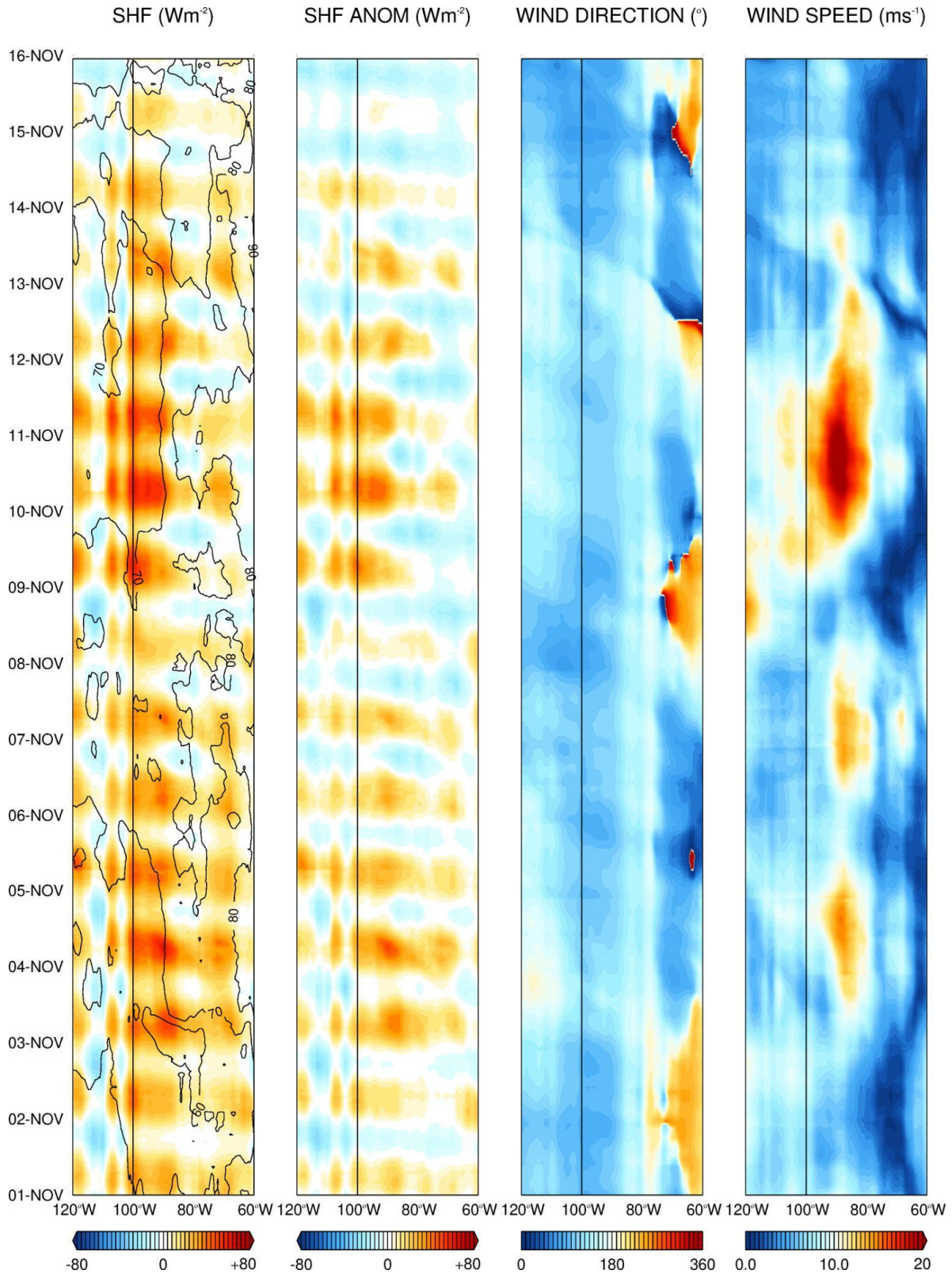
Figure 6: **November 2011 Foehn events:** Integrated Water Vapour Transport (IVT; kgm[-2]; shading) standardized anomalies with respect to ERA-5's 1979-2020 monthly climatology, the vectors give a one standard deviation

anomaly and are only plotted if the IVT standardized anomalies exceed one, and 500 hPa geopotential height standardized anomalies (solid contours) on (a) 10 November and (b) 11 November 2011 at 00 UTC. The thin and thick green lines denote the 90th and 99th IVT percentiles, respectively, the yellow star gives the location of the Evans Knoll weather station (-74.85ºS; -100.404ºW), and the red solid line is the 0ºC 2-m temperature isotherm. (c) 10-m wind speed (shading; m s^{-1}), with the 90th and 99th percentiles denoted by the solid thin and thick green lines, respectively, and 10-m winds (vectors; m s^{-1}) on 11 November 2011 at 06 UTC. The grey lines are orographic contours drawn and labelled every 500 m, and the dark solid purple and pink lines highlight regions where the sea-ice concentration is equal to 0% and 85%, respectively. (d) is as (c) but with the shading giving the sensible heat flux (shading; W m^{-2}), positive if downwards towards the surface. The anomalies and percentile ranks for the IVT, 10-m horizontal winds, 500 hPa geopotential height and 2-m temperature are calculated from the distribution of all 3-h values within +/- 15 Julian days from the given date during the 1979–2020 period and at a given grid point. (e) Hovmoeller plot of sensible heat flux (shading; W m^{-2}) and relative humidity (contours, every 10%), sensible heat flux anomalies with respect to the 1979-2021 climatology (W m^{-2}), and 10-m wind direction (º) and speed (m s^{-1}) for 01-15 November 2011. The fields are averaged over 72.5º-77.5ºS and are plotted for the region 120ºW-60ºW. All colour bars are linear with only the lowest, middle and highest values shown. The black vertical line indicates the approximate longitude of PIG (100ºW).

550
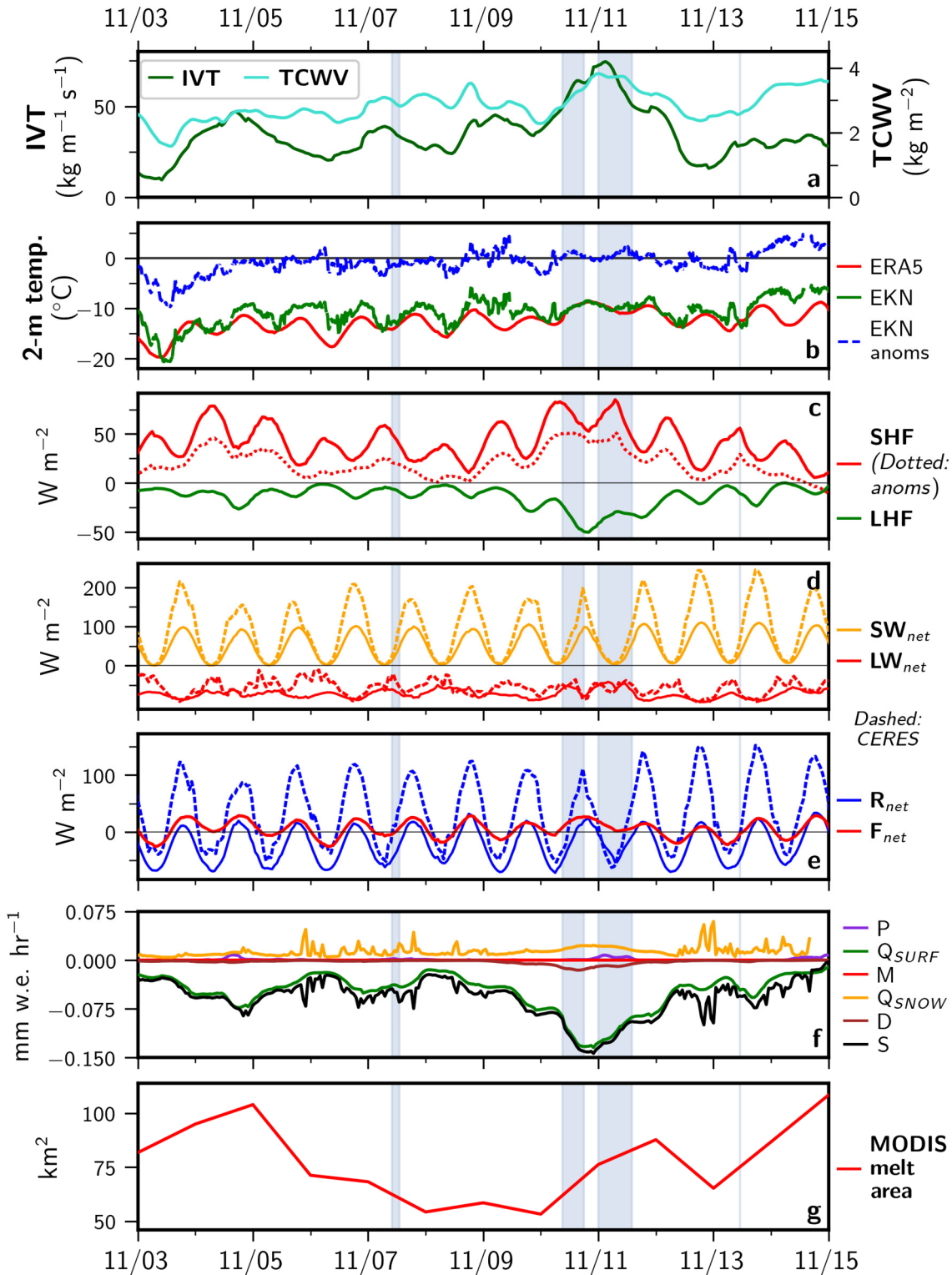
Figure 7: **Impacts of Foehn winds on ice:** Time series of 1-hourly ERA-5 variables averaged over PIG (red box in Fig. 1a) from 03 to 14 November 2011: (a) Integrated water vapor transport (IVT; light green; kg m⁻¹ s⁻¹) and total column water vapor (TCWV; dark green; kg m⁻²); (b) 10-min observed 2-m temperature (green; ⁰C) at the Evans Knoll weather station (-74.85ºS, -100.404ºW; 188 m above sea-level), the anomalies with respect to the 2011-2015

hourly climatology are given by the dashed blue line, and area-averaged ERA-5 2-m temperature (red; ºC); (c) ERA-5 sensible heat flux (SHF; red; W m^{-2}) and latent heat flux (LHF; orange; W m^{-2}); (d) net shortwave radiation (SW_{net}; orange; W m^{-2}) and longwave radiation (LW_{net}; red; W m^{-2}) flux at the surface; (e) net radiation (R_{net}; blue; W m^{-2}) and total energy flux ($F_{net} = SHF + LHF + R_{net}$; red; W m^{-2}) at the surface; (f) individual components of the surface mass balance, Eq. (2), expressed in mm w.e. hr^{-1}. The S, P, M, Q_{surf}, Q_{snow} and D terms are given by the black, purple, red, green, orange and brown lines, respectively; (g) Daily total surface area (km^2) of melt ponds observed from MODIS imagery. In panel (c), the SHF anomalies, calculated as the difference from the domain-averaged 1979-2020 November hourly monthly mean, are also plotted. In (d)-(e), the net radiative variables from CERES averaged over the same domain are plotted as dashed lines for comparison. Times when Foehn occurred are shaded in blue.

6. Discussion and Conclusions

Pine Island Glacier (PIG), located in West Antarctica around 75ºS and 100ºW between the Antarctic Peninsula to the east and the Ross Ice Shelf to the west, has been losing ice mass at an accelerated rate over the last two decades. While the vast majority of the studies on ice loss at PIG focus on ocean dynamics (e.g. Stanton et al., 2013; Favier et al., 2014), atmospheric forcing is also likely to be important, with warmer and more moist air intrusions from the mid-latitudes and Foehn effects the likely candidates (Ghiz et al., 2021). The role of moist air intrusions is well documented (e.g. Willie et al., 2021), but less attention has been paid to Foehn, in particular around PIG where the complex terrain promotes its occurrence. Foehn effects can lead to ice loss through sublimation, which is typically a small-scale and invisible phenomenon in nature and hence difficult to be detected using satellite data. At the same time, Foehn plays an important role in the surface mass balance around Antarctica (Ghiz et al., 2021), and a better understanding of its occurrence may help to reduce the major uncertainties that still exist (The IMBIE team, 2018). In this work, a 41-year climatology of Foehn events at PIG is generated using ERA-5 reanalysis data, and its impact on the surface mass balance is analyzed. The large-scale atmospheric circulation patterns that favor Foehn events at PIG are also identified.

Foehn events at PIG are more frequent in the colder months from June to October, with an average of 3.0 events per month in the 105º-95ºW and 70º-80ºS region in August 1980-2020 and just 0.37 in January. The peak in austral winter is consistent with the poleward position of the mid-latitude storm track, with the Amundsen Sea Low (ASL), a semi-permanent low pressure in the Amundsen-Bellingshausen Seas, closest to the Antarctica coast in late winter. The presence of a low just north of PIG favours easterly to southeasterly winds at the site, which encourages the occurrence of Foehn. The duration of Foehn events exhibits a less pronounced annual cycle, with Foehn episodes typically lasting 5 to 9 h. The negative phase of the Antarctic Oscillation, in particular in the cold season (May to August), and the positive phase of the Southern Annular Mode, foster the occurrence of Foehn at PIG. The former is a more indirect pathway, with the air flow coming from the Weddell sector and moving over the Ellsworth Land before reaching PIG, while in the latter the air mass comes from the Pacific Ocean and flows over the high terrain directly to the northeast of PIG before descending into the glacier basin.

A composite of Foehn and no-Foehn episodes revealed that Foehn events have an important impact on the surface mass balance. It is concluded that surface sublimation plays the major role, with a magnitude of ~1.434 mm water equivalent (w.e.) day^{-1}, comparable to that observed at other sites in Antarctica. The blowing snow sublimation and divergence rate have a comparable magnitude to that of the precipitation (snowfall) rate, with values of 0.35-0.36 mm w.e. day^{-1}. However, while the former makes a positive contribution to the surface mass balance due to the convergence of the snow transport rate at the glacier basin, the latter depletes surface snow, as the drier conditions associated with Foehn reduce the likelihood of the occurrence of precipitation. The melting rate is negligible and is restricted to the coastal areas to the north of the glacier.

A particularly strong Foehn event took place on 09-11 November 2011. During this period the ASL was more than 1.5 standard deviations stronger than the 1979-2020 climatological mean, with an atmospheric river from the Southeast Pacific injecting moisture into West Antarctica through the Weddell Sea. As the southeasterly winds descended the high terrain east and southeast of the glacier they accelerated, with 10-m wind speeds in excess of 20 m s^{-1} and in the top 10% of the climatological distribution, and downward sensible heat fluxes higher than 75 W m^{-2}, a clear signature of Foehn effects. Besides surface sublimation, at a rate of up to 0.13 mm w.e. hr^{-1}, melting was detected using satellite data with the hourly melting area at times in excess of 100 km^2.

As Foehn has been shown to play an important role in modulating ice conditions elsewhere around Antarctica such as in the Antarctic Peninsula (Massom et al., 2018) and Ross Ice Shelf (Zou et al. 2021a and b), a detailed analysis of Antarctica-wide Foehn occurrence is needed to better quantify its contribution to snow sublimation and ice loss. The fact that Foehn winds are more effective in inducing snow sublimation than snow melt at PIG, makes it challenging to detect their total impact on the ice state at the scale of the continent as snow evaporation cannot be detected from space. Advanced remote sensing techniques to detect changes in the depth of the snow layer over land ice are therefore needed.

Acknowledgment

The authors wish to acknowledge the contribution of Khalifa University's high-performance computing and research computing facilities to the results of this research. This work has been supported by Masdar Abu Dhabi Future Energy Company through research grant number 8434000222. We also appreciate the support of the University of Wisconsin-Madison Automatic Weather Station Program for the data set and information, NSF grant number 1924730. We would like to thank the two anonymous reviewers for their insightful and constructive comments and suggestions that have substantially improved the quality of this manuscript.

Code Availability

The scripts used to process MODIS data and estimate the melting area are available upon request from Dr. Catherine Walker (catherine.c.walker@nasa.gov). The codes used to estimate the terms in the surface mass balance can be requested from Prof. Diana Francis (diana.francis@ku.ac.ae).

Data Availability

All the data used to generate the figures in this study has been uploaded to Francis et al. (2023). ERA-5 hourly reanalysis surface (Hersbach et al. 2018b) and pressure-level (Hersbach et al. 2018a) data used in this work is freely available online on Copernicus' Climate Change Service Climate Data Store website. The weather data for the Evans Knoll station located next to Pine Island Glacier (PIG) is freely available at the Antarctic Meteorological Research Center & Automatic Weather Stations Project website (Lazzara et al., 2022). The Antarctic 1 km Digital Elevation Model (DEM) from Combined ERS-1 Radar and ICESat Laser Satellite Altimetry, Version 1 (NSIDC-0422; Bamber et al. 2009a) used to plot Antarctica surface elevation, MEaSUREs InSAR-Based Antarctica Ice Velocity Map, Version 2 (NSIDC-0484; Rignot et al. 2017) used to plot mean ice velocity of Pine Island and Thwaites Glaciers, and MEaSUREs Antarctic Boundaries for IPY 2007-2009 from Satellite Radar, Version 2 (NSIDC-0709; Mouginot et al. 2017) are freely available available from the National Aeronautics and Space Administration National Snow and Ice Data Center (NSIDC) Distributed Active Archive Center website. The Clouds and Earth's Radiant Energy System (CERES) surface fluxes product SYN1deg - Level 3 has been made publicly available at NASA/LARC/SD/ASDC (2017). Sentinel-2 satellite data, used to extract the sea-ice front at PIG, is available online at (Copernicus, 2022). The MODIS daily global surface reflectance Level 3 data (MOD09CMG, MYD09CMG; Vermote 2015a,b) are publicly available from NASA Earthdata. The figures presented in this paper were generated using the Interactive Data Language (IDL; Bowman, 2005) software version 8.8.1 and the Matplotlib (Hunter, 2007) and Cartopy (Met Office, 2014) python libraries.

Author Contribution

DF conceived the study. RF and DF wrote the manuscript with inputs from KSM, SL and CW. SL and CW processed the MODIS data while RF and KSM analyzed the reanalysis data. DF provided formal analysis and validation of the results.

Conflict of Interest

SL is a member of the editorial board of The Cryosphere and this is handled according to the journal policies.

References

Adusumilli, S., Fish, M. A., Fricker, H. and Medley, B. (2021) Atmospheric river precipitation contributed to rapid increases in surface height of the West Antarctic Ice Sheet in 2019. Geophysical Research Letters, 48, e2020GL091076. https://doi.org/10.1029/2020GL091076.

Aulicino, G., Sansiviero, M., Paul, S., Cesarano, C., Fusco, G., Wadhams, P., Budillon, G. (2018) A New Approach for Monitoring the Terra Nova Bay Polynya through MODIS Ice Surface Temperature Imagery and Its Validation during 2011 and 2011 Winter Seasons. Remote Sensing, 10, 366. https://doi.org/10.3390/rs10030366.

[Dataset] Bamber, J., Gomez-Dans, J. L. and Griggs, J. A. (2009a) Antarctic 1km Digital Elevation Model (DEM) from Combined ERS-1 Radar and ICESat Laser Satellite Altimetry, version 1. Boulder, Colorado USA. National Aeronautics and Space Administration National Snow and Ice Data Center Distributed Active Archive Center. Accessed on 26 April 2022, available online at https://doi.org/10.5067/H0FQ1KL9NEKM.

Bamber, J. L., Riva, R. E. M., Vermeersen, B. L. A. and LeBrocq, A. M. (2009b) Reassessment of the potential sea-level rise from a collapse of the West Antarctic Ice Sheet. Science, 324, 901-903. https://doi.org/10.1126/science.1169335.

Bell, R. E., Banwell, A. F., Trusel, L. D. and Kingslake, J. (2018) Antarctic surface hydrology and impacts on ice-sheet mass balance. Nature Climate Change, 8, 1044-1052. https://doi.org/10.1038/s41558-018-0326-3.

Bowman, K. P. (2005) An Introduction to Programming with IDL: Interactive Data Language [Software]. Academic Press, 304 pp., ISBN-10: 012088559X, ISBN-13: 978-0120885596.

Bozkurt, D., Rondanelli, R., Marin, J. C. and Garreaud, R. (2018) Foehn event triggered by an atmospheric river underlies record-setting temperature along continental Antarctica. Journal of Geophysical Research: Atmospheres, 123, 3871-3892. https://doi.org/10.1002/2017JD027796.

Bromwich, D. H. (1989) Satellite Analysis of Antarctic Katabatic Wind Behavior. Bulletin of the American Meteorological Society, 70, 738-749. https://doi.org/10.1175/1520-0477(1989)070<0738:SAOAKW>2.0.CO;2.

[Dataset] Copernicus (2022) Copernicus Open Access Hub. Available online at https://scihub.copernicus.eu/, accessed on 10 October 2022.

Das, I., Bell, R. E., Scambos, T. A., Wolovick, M., Creyts, T. T., Studinger, M., Frearson, N., Nicolas, P., Lenaerts, J. T. M. and van den Broeke, M. (2013) Influence of persistent wind scour on the surface mass balance of Antarctica. Nature Geoscience, 6, 367-371. https://doi.org/10.1038/ngeo1766.

Datta, R. T., Tedesco, M., Fettweis, X., Agosta, C., Lhermitte, S., Lenaerts, J. T. M., Wever, N. (2019) The effect of Foehn-induced surface melt on firn evolution over the northeast Antarctic peninsula. Geophysical Research Letters, 46, 3822-3831. https://doi.org/10.1029/2018GL080845.

De Rydt, J., Reese, R., Paolo, F. S. and Gudmundsson, G. H. (2021) Drivers of Pine Island Glacier speed-up between 1996 and 2016. The Cryosphere, 15, 113-132. https://doi.org/10.5194/tc-15-113-2021.

Dery, S. J., Yau, M. K. (1999) A Bulk Blowing Snow Model. Boundary-Layer Meteorology, 93, 237-251. https://doi.org/10.1023/A:1002065615856.

Dery, S. J., Yau, M. K. (2002) Large-scale mass balance effects of blowing snow and surface sublimation. Journal of Geophysical Research, 107, 4679. https://doi.org/10.1029/2001JD001251.

Dias da Silva, P. E., Hodges, K. I., Coutinho, M. M. (2021) How well does the HadGEM2-ES coupled model represent the Southern Hemisphere storm tracks? Climate Dynamics, 56, 1145-1162. https://doi.org/10.1007/s00382-020-05523-9.

Dirscherl, M. C., Dietz, A. J., Kuenzer, C. (2021) Seasonal evolution of Antarctic supraglacial lakes in 2015-2021 and links to environmental controls. The Cryosphere, 15, 5205-5226. https://doi.org/10.5194/tc-15-5205-2021.

Djoumna, G. and Holland, D. M. (2021) Atmospheric rivers, warm air intrusions, and surface radiation balance in the Amundsen Sea Embayment. Journal of Geophysical Research: Atmospheres, 126, e2020JD034119. https://doi.org/10.1029/2020JD034119.

Doelling, D. R., Loeb, N. G., Keyes, D. F., Nordeen, M. L., Morstad, D., Nguyen, C., Wielicki, B. A., Young, D. F. and Sun, M. (2013) Geostationary Enhanced Temporal Interpolation for CERES Flux Products. Journal of Atmospheric and Oceanic Technology, 30, 1072-1090. https://doi.org/10.1175/JTECH-D-12-00136.1.

Doelling, D. R., Sun, M., Nguyen, L. T., Nordeen, M. L., Haney, C. O., Keyes, D. F. and Mlynczak, P. E. (2016) Advances in Geostationary-Derived Longwave Fluxes for the CERES Synoptic (SYN1deg) Product. Journal of Atmospheric and Oceanic Technology, 33(3), 503-521. https://doi.org/10.1175/JTECH-D-15-0147.1.

Donat-Magnin, M., Jourdain, N. C., Kittel, C., Agosta, C., Amory, C., Gallee, H, Kinner, G., Chekki, M. (2021) Future surface mass balance and surface melt in the Amundsen sector of the West Antarctic Ice Sheet. The Cryosphere, 15, 571-593. https://doi.org/10.5194/tc-15-571-2021.

ECMWF (2016) IF Documentation - Cy43r1 Operational Implementation 22 Nov 2016. Part IV: Physical Processes. Accessed on 26 October 2022, available online at https://www.ecmwf.int/sites/default/files/elibrary/2016/17117-part-iv-physical-processes.pdf.

735 Elvidge, A. D., Kuipers Munneke, P., King, J. C., Renfrew, I. A., Gilbert, E. (2020) Atmospheric drivers
736 of melt on Larsen C Ice Shelf: Surface energy budget regimes and the impact of foehn. Journal of
737 Geophysical Research: Atmospheres, 125, e2020JD032463. https://doi.org/10.1029/2020JD032463.

739 Elvidge, A. D. and Renfrew, I. A. (2016) The Causes of Foehn Warming in the Lee of Mountains. Bulletin
740 of the American Meteorological Society, 97(3), 455-466. https://doi.org/10.1175/BAMS-D-14-00194.1.

742 Elvidge, A. D., Renfrew, I. A., King, J. C., Orr, A., Lachlan-Cope, T. A. (2016) Foehn warming
743 distributions in nonlinear and linear flow regimes: a focus on the Antarctic Peninsula. Quarterly Journal of
744 the Royal Meteorological Society, 142, 618-631. https://doi.org/10.1002/qj.2489.

746 Favier, L., Durand, G., Cornford, S. L., Gudmundsson, G. H., Gagliardini, O., Gillet-Chaulet, F., Zwinger,
747 T., Payne, A. J. and Le Brocq, A. M. (2014) Retreat of Pine Island Glacier controlled by marine ice-sheet
748 instability. Nature Climate Change, 4, 117-121. https://doi.org/10.1038/nclimate2094.

750 Feldmann, J., Levermann, A., Mengel, M. (2019) Stabilizing the West Antarctic Ice Sheet by surface mass
751 deposition. Science Advances, 5. https://doi.org/10.1126/sciadv.aaw4132.

753 Fogt, R. L. and Marshall, G. J. (2020) The Southern Annular Mode: Variability, trends, and climate impacts
754 across the Southern Hemisphere. WIREs Climate Change, 11, e625. https://doi.org/10.1002/wcc.652.

756 Francis, D., Fonseca, R., Mattingly, K., Lhermitte, S. and Walker, C. (2023) Datasets for the publication
757 "Foehn Winds at Pine Island Glacier and its role in Ice Shelf Sublimation and Surface Melt" [Dataset].
758 Zenodo, https://zenodo.org/record/7707591.

760 Francis, D., Fonseca, R., Mattingly, K. S., Marsh, O. J., Lhermitte, S. and Cherif, C. (2022) Atmospheric
761 triggers of the Brunt Ice Shelf calving in February 2021. Journal of Geophysical Research: Atmospheres,
762 127, e2021JD036424. https://doi.org/10.1029/2021JD036424.

764 Francis, D., Mattingly, K. S., Lhermitte, S., Temimi, M. and Heil, P. (2021) Atmospheric extremes caused
765 high oceanward sea surface slope triggering the biggest calving event in more than 50 years at the Amery
766 Ice Shelf. The Cryosphere, 15, 2147-2165. https://doi.og/10.5194/tc-15-2147-2021.

768 Francis, D., Mattingly, K. S., Temimi, M., Massom, R. and Heil, P. (2020) On the crucial role of
769 atmospheric rivers in the two major Weddell Polynya events in 1973 and 2017 Antarctica. Science
770 Advances, 6, eabc2695. https://doi.org/10.1126/sciadv.abc2695.

772 Gehring, J., Vignon, E., Billaut-Roux, A.-C., Ferrone, A., Protat, A., Alexander, S. P., Berne, A. (2022)
773 Orographic flow influence on precipitation during an atmospheric river event at Davis, Antarctica. Journal
774 of Geophysical Research: Atmospheres, 127, e2021JD035210. https://doi.org/10.1029/2021JD035210.

776 Ghiz, M. K., Scott, R. C., Vogelmann, A. M., Lenaerts, J. T. M., Lazzara, M. and Lubin, D. (2021) Energetic
777 of surface melt in West Antarctica. The Cryosphere, 15, 3459-3494. https://doi.org/10.5194/tc-15-3459-
778 2021.

779

780 Gong, D. and Wang, S. (1999) Definition of Antarctic oscillation index. Geophysical Research Letters,
781 26(4), 459-462. https://doi.org/10.1029/1999GL900003.

782

783 Gonzalez, S., Vasallo, F., Sanz, P., Quesada, A. and Justel, A. (2021) Characterization of the summer
784 surface mesoscale dynamics at Dome F, Antarctica. Atmospheric Research, 259, 105699.
785 https://doi.org/10.10.1016/j.atmosres.2021.105699.

786

787 Gossart, A., Helsen, S., Lenaerts, J. T. M., Vanden Broucke, S., van Lipzig, N. P. M. and Souverijns, N.
788 (2019) An Evaluation of Surface Climatology in State-of-the-Art Reanalyses over the Antarctic Ice Sheet.
789 Journal of Climate, 32(20), 6899-6915. https://doi.org/10.1175/JCLI-D-19-0030.1.

790

791 Goyal, R., Jucker, M., Gupta, A. S., Hendon, H. H. and England, M. H. (2021) Zonal wave 3 pattern in the
792 Southern Hemisphere generated by tropical convection. Nature Geosciences, 14, 732-738.
793 https://doi.org/10.1038/s41561-021-00811-3.

794

795 Greene, C. A., Gardner, A. S., Schlegel, N.-J. and Fraser, A. D. (2022) Antarctic calving loss rivals ice-
796 shelf thinning. Nature, 609, 948-953. https://doi.org/10.1038/s41586-022-050307-w.

797

798 [Dataset] Hersbach, H., Bell, B., Berrisford, P., Biavati, G., Horanyi, A., Munoz Sabater, J., Nicolas, J.,
799 Peubey, C., Radu, R., Rozum, I., Schepers, D., Simmons, A., Soci, C., Dee, D. and Thepaut, J.-N. (2018a)
800 ERA5 hourly data on pressure levels from 1959 to present. Copernicus Climate Change Service (C3S)
801 Climate Data Store (CDS). https://doi.org/10.24381/cds.bd0915c6.

802

803 [Dataset] Hersbach, H., Bell, B., Berrisford, P., Biavati, G., Horanyi, A., Munoz Sabater, J., Nicolas, J.,
804 Peubey, C., Radu, R., Rozum, I., Schepers, D., Simmons, A., Soci, C., Dee, D. and Thepaut, J.-N. (2018b)
805 ERA5 hourly data on single levels from 1959 to present. Copernicus Climate Change Service (C3S) Climate
806 Data Store (CDS). https://doi.org/10.24381/cds.adbb2d47.

807

808 Hofsteenge, M. G., Cullen, N. J., Reijmer, C., van den Broeke, M., Katurji, M., Orwin, J. F. (2022) The
809 surface energy balance during foehn events at Joyce Glacier, McMurdo Dry Valleys, Antarctica. The
810 Cryosphere, 16, 5041-5059. https://doi.org/10.5194/tc-16-5041-2022.

811

812 Holland, P. R., Brisbourne, A., Corr, H. F. J., McGrath, D., Purdon, K., Paden, J., Fricker, H. A., Paolo, F.
813 S. and Fleming, A. H. (2015) Oceanic and atmospheric forcing of Larsen C Ice-Shelf thinning. The
814 Cryosphere, 9, 1005-1024. https://doi.org/10.5194/tc-9-1005-2015.

815

816 Holland, P. R., Feltham, D. L., Jenkins, A. (2007) Ice Shelf Water plume flow beneath Filchner-Ronne Ice
817 Shelf, Antarctica. Journal of Geophysical Research, 112, C05044. https://doi.org/10.1029/2006JC003915.

818

819 [Dataset] Hunter, J. D. (2007) Matplotlib: A 2D graphics environment . Computing in Science and
820 Engineering, 9, 90-95. https://doi.org/10.1109/MSCE.2007.55.

821

822   Hoskins, B. J. and Karoly, D. J. (1981) The Steady Linear Response of a Spherical Atmosphere to Thermal
823   and Orographic Forcing. Journal of Atmospheric Sciences, 38(6), 1179-1996. https://doi.org/10.1175/1520-
824   0469(1981)038<1179:TSLROA>2.0.CO;2.

826   Jenkins, A., Dutrieux, P., Jacobs, S. S., McPhail, S. D., Perrett, J. R., Webb, A. T. and White, D. (2010)
827   Observations beneath Pine Island Glacier in West Antarctica and implications for its retreat. Nature
828   Geosciences, 3, 468-472. https://doi.org/10.1038/ngeo890.

830   Joughin, I., Shapero, D., Smith, B., Dutrieux, P. and Barham, M. (2021) Ice-shelf retreat drives recent Pine
831   Island Glacier speedup. Science Advances, 7(24). https://doi.org/10.1126/sciadv.abg3080.

833   Kaufman, Y. J., Tanre, D., Rmer, L. A., Vermote, E. F., Chu, A. and Holben, B. N. (1997) Operational
834   remote sensing of tropospheric aerosol over land from EOS moderate resolution imaging spectroradiometer.
835   Journal of Geophysical Research, 192, 17051-17067. https://doi.org/10.1029/96JD03988.

837   Kirchgaessner, A., King, J. C. and Anderson, P. S. (2021) The impact of Fohn conditions across the
838   Antarctic Peninsula on local meteorology based on AWS measurements. Journal of Geophysical Research:
839   Atmospheres, 126, e2020JD033748. https://doi.org/10.1029/2020JD033748.

841   Konrad, H., Hogg, A., Mulvaney, R., Arthern, R., Tuckwell, R., Medley, B., Shepherd, A. (2019)
842   Observations of surface mass balance on Pine Island Glacier, West Antarctica, and the effect of strain
843   history in fast-flowing sections. Journal of Glaciology, 65, 595-604. https://doi.org/10.1017/jog.2019.36.

845   Kowalewski, S., Helm, V., Morris, E. M. and Eisen, O. (2021) The regional-scale surface mass balance of
846   Pine Island Glacier, West Antarctica, over the period 2005-2014, derived from airborne radar soundings
847   and neutron probe measurements. The Crysophere, 15, 1285-1305. https://doi.org/10.5194/tc-15-1285-201.

849   Laffin, M. K., Zender, C. S., Singh, S., Van Wessem, J. M., Smeets, C. J. P. P. and Reijmer, C. H. (2021)
850   Climatology and evolution of the Antarctic Peninsula fohn wind-induced melt regime from 1979-2018.
851   Journal   of   Geophysical   Research: Atmospheres,   126,   e2020JD033682.
852   https://doi.org/10.1029/2020JD033682.

854   [Dataset] Lazzara, M. (2022) Antarctic Meteorological Research Center & Automatic Weather Stations
855   Project. Accessed on 06 November 2022, available online at http://amrc.ssec.wisc.edu/.

857   Lhermitte, S., Sun, S., Shuman, C., Wouters, B., Pattyn, F., Wuite, J., Berthier, E. and Nagler, T. (2021)
858   Damage accelerates ice shelf instability and mass loss in Amundsen Sea Embayment. Proceeding of the
859   National Academy of Sciences of the United States of America, 117(40), 24735-24741.
860   https://doi.org/10.1073/pnas.1912890117.

862   Lestari, R. K. and Koh, T.-Y. (2016) Statistical Evidence for Asymmetry in ENSO-IOD Interactions.
863   Atmosphere-Ocean, 54(5), 498-504. https://doi.org/10.1080/07055900.2016.1211084.
864

865 Li, S., Liao, J. and Zhang, L. (2022) Extraction and analysis of elevation changes in Antarctic ice sheet
866 from CryoSat-2 and Sentinel-3 radar altimeters. Journal of Applied Remote Sensing, 16(3), 034514.
867 https://doi.org/10.1117/1.JRS.16.034514.

869 Liu, S., Su, S., Cheng, Y., Tong, X. and Li, R. (2022) Long-Term Monitoring and Change Analysis of Pine
870 Island Ice Shelf Based on Multi-Source Satellite Observations during 1973-2020. Journal of Marine Science
871 and Engineering, 10, 976. https://doi.org/10.3390/jmse10070976.

873 Marshall, G. J. (2003) Trends in the Southern Annular Mode from observations and reanalyses. Journal of
874 Climate, 16, 4134-4143. https://doi.org/10.1175/1520-
875 0442%282003%29016<4134%3ATITSAM>2.0.CO%3B2.

877 Massom, R. A., Scambos, T. A., Bennetts, L. K., Reid, P., Squire, V. A. and Stammerjohn, S. E. (2018)
878 Antarctic ice shelf disintegration triggered by sea ice loss and ocean swell. Nature, 558, 383-389.
879 https://doi.org/10.1038/s41586-018-0212-1.

881 MacDonald, M. K., Pomeroy, J. W., Essery, R. L. H. (2018) Water and energy fluxes over northern prairies
882 as affected by chinook winds and winter precipitation. Agricultural and Forest Meteorology, 248, 372-385.
883 https://doi.org/10.1016/j.agrformet.2017.10.025.

885 Mclennan, M. L. and Lenaerts, J. T. M. (2021) Large-scale atmospheric drivers of snowfall over Thwaites
886 Glacier, Antarctica. Geophysical Research Letters, 48, e2021GL093644.
887 https://doi.org/10.1029/2021GL093644.

889 [Dataset] Met Office (2014) Cartopy: a cartographic python library with a Matplotlib interface. Accessed
890 on 29 June 2022, available online at https://scitools.org.uk/cartopy.

892 Miles, B. W. J., Stokes, C. R. and Jamieson, S. S. R. (2017) Simultaneous disintegration of outlet glaciers
893 in Porpoise Bay (Wilkes Land), East Antarctica, driven by sea ice break-up. The Cryosphere, 11, 427-442.
894 https://doi.org/10.5194/tc-11-427-2017.

896 Moncada, J. M. and Holland, D. M. (2019) Automatic Weather Station Pine Island Glacier. United States
897 Antarctic Program (USAP) Data Center. Accessed on 26 April 2022, https://doi.org/10.15784/601216.

899 Montesi, J., Elder, K., Schmidt, R. A., David, R. E. (2004) Sublimation of Intercepted Snow within a
900 Subalpine Forest Canopy at Two Elevations. Journal of Hydrometeorology, 5, 763-773.
901 https://doi.org/10.1175/1525-7541(2004)005<0763:SOISWA>2.0.CO;2.

903 Mottram, R., Hansen, N., Kittel, C., van Wessem, J. M., Agosta, C., Amory, C., Boberg, F., van de Berg,
904 W., Fettweis, X., Gossart, A., van Lipzig, N. P. M., van Mejigaard, E., Orr, A., Phillips, T., Webster, S.,
905 Simonsen, S. B. and Souverijns, N. (2021) What is the surface mass balance of Antarctica? An
906 intercomparison of regional climate model estimates. The Cryosphere, 15, 3751-3784.
907 https://doi.org/10.5194/tc-15-3751-2021.

908

909 [Dataset] Mouginot, J., B. Scheuchl, and E. Rignot. 2017. MEaSUREs Antarctic Boundaries for IPY 2007-
910 2009 from Satellite Radar, Version 2. Boulder, Colorado USA. NASA National Snow and Ice Data Center
911 Distributed Active Archive Center. https://doi.org/10.5067/AXE4121732AD. Accessed on 8 November
912 2022.
913

914 Moussavi, M. S., Abdalati, W., Pope, A., Scambos, T., Tedesco, M., MacFerrin, M. and Grigsby, S. (2016)
915 Derivation and validation of supraglacial lake volumes on the Greenland Ice Sheet from high-resolution
916 satellite imagery. Remote Sensing of Environment, 183, 294-303.
917 https://doi.org/10.1016/j.rse.2016.05.024.
918

919 [Dataset] NASA (National Aeronautics and Space Administration) / LARC (Langley Research Center) /
920 SD (Science Division) / ASDC (Atmospheric Data Center) (2017) CERES and GEO-Enhanced TOA,
921 Within-Atmosphere and Surface Fluxes, Clouds and Aerosols 1-Hourly Terra-Aqua Edition4A. NASA
922 Langley Atmospheric Science Data Center DAAC. Retrieved from
923 https://doi.org/10.5067/TERRA+AQUA/CERES/SYN1DEG-1HOUR_L3.004A.
924

925 Nilsson, J., Gardner, A. S. and Paolo, F. S. (2022) Elevation change of the Antarctic Ice Sheet: 1985 to
926 2020. Earth System Science Data, 14, 3573-3598. https://doi.org/10.5194/essd-14-3573-2022.
927

928 Orr, A., Deb, P., Clem, K. R., Gilbert, E., Bromwich, D. H., Boberg, F., Colwell, S., Hansen, N., Lazzara,
929 M. A., Mooney, P. A., Mottram, R., Niwano, M., Phillips, T., Pishniak, D., Reijmer, C. H., van de Berg,
930 W. J., Webster, S. and Zuo, X. (2022) Characteristics of surface "melt potential" over Antarctic ice shelves
931 based on regional atmospheric model simulations of summer air temperature extremes from 1979/80 to
932 2018/19. Journal of Climate, 1-61. https://doi.org/10.1175/JCLI-D-22-0386.1.
933

934 Pohl, B., Fauchereau, N., Reason, C. J. C. and Rouault, M. (2010) Relationships between the Antarctic
935 Oscillation, the Madden-Julian Oscillation, and ENSO, and Consequences for Rainfall Analysis. Journal of
936 Climate, 23(2), 238-254. https://doi.org/10.1175/2009JCLI2443.1.
937

938 Polvani, L. M., Banerjee, A., Chemke, R., Doddridge, E. W., Ferreira, D., Gnanadesikan, A., Holland, M.
939 A., Kostov, Y., Marshall, J., Seviour, W. J. M., Solomon, S. and Waugh, D. W. (2021) Interannual SAM
940 modulation of Antarctic sea ice extent does not account for its long-term trends, pointing to a limited role
941 for ozone depletion. Geophysical Research Letters, 48, e2021GL098471.
942 https://doi.org/10.1029/2021GL094871.
943

944 Ponti, S., Scipionotti, R., Pierattini, S., Guglielmin, M. (2021) The Spatio-Temporal Variability of Frost
945 Blisters in a Perennial Frozen Lake along the Antarctic Coast as Indicator of the Goundwater Supply.
946 Remote Sensing, 13, 435. https://doi.org/10.3390/rs13030435.
947

948 Pradhananga, D., Pomeroy, J. W. (2022) Diagnosing changes in glacier hydrology from physical principles
949 using a hydrological model with snow redistribution, sublimation, firnification and energy balance ablation
950 algorithms. Journal of Hydrology, 608, 127545. https://doi.org/10.1016/j.jhydrol.2022.127545.
951

Quintanar, A. I. and Mechoso, C. R. (1995a) Quasi-Stationary Waves in the Southern Hemisphere. Part I: Observational Data. Journal of Climate, 8(11), 2659-2672. https://doi.org/10.1175/1520-0442(1995)008<2659:QSWITS>2.0.CO;2.

Quintanar, A. I. and Mechoso, C. R. (1995b) Quasi-Stationary Waves in the Southern Hemisphere. Part II: Generation Mechanisms. Journal of Climate, 8(11), 2673-2690. https://doi.org/10.1175/1520-0442(1995)008<2673.QSWITS>2.0.CO;2.

Raphael, M. N., Marshall, G. J., Turner, J., Fogt, R. L., Schneider, D., Dixon, D. A., Hosking, J. S., Jones, J. M. and Hobbs, W. R. (2016) The Amundsen Sea Low: Variability, Change, and Impact on Antarctic Climate. Bulletin of the American Meteorological Society, 97(1), 111-121. https://doi.org/10.1175/BAMS-D-14-00018.1.

Reijmer, C., Greuell, W. and Oerlemans, J. (1999) The annual cycle of meteorological variables and the surface energy balance on Berkner Island, Antarctica. Annals of Glaciology, 29, 49-54. https://doi.org/10.3189/172756499781821166.

[Dataset] Rignot, E., Mouginot, J. and Scheuchl, B. (2017) MEaSUREs InSAR-Based Antarctica Ice Velocity Map, Version 2. Boulder, Colorado USA. National Aeronautics and Space Administration National Snow and Ice Data Center Distributed Active Archive Center. Accessed on 26 April 2022, available online at https://doi.org/10.5067/D7GK8F5J8M8R.

Rintoul, S. R., Silvano, A., Pena-Molino, B., Wijk, E. V., Rosenberg, M., Geenbaum, J. E., Blankenship, D. (2016) Ocean heat drives rapid basal melt of the Totten Ice Shelf. Science Advances, 2. https://doi.org/10.1126/sciadv.1601610.

Rogers, R. R., Yau, M. K. (1989) A Short Course in Cloud Physics, 3rd edition. Pergamon, New York, 293 pp.

Rosier, S. H. R., Reese, R., Donges, J. F., De Rydt, J., Gudmundsson, G. H. and Winkelmann, R. (2021) The tipping points and early warning indicators for Pine Island Glacier, West Antarctica. The Cryosphere, 15, 1501-1516. https://doi.org/10.5194/tc-15-1501-2021.

Rousseeux, P. J. (1987) Silhouettes: A graphical aid to the interpretation and validation of cluster analysis. Journal of Computational and Applied Mathematics, 20, 53-65. https://doi.org/10.1016/0377-0427(87)90125-7.

Scarchilli, C., Frezzotti, M., Grigioni, P., De Silvestri, L., Agnoletto, L., Dolci, S. (2010) Extraordinary blowing snow transport events in East Antarctica. Climate Dynamics, 34, 1195-1206. https://doi.org/10.1007/s00382-009-0601-0.

Scott, R. C., Nicolas, J. P., Bromwich, D. H., Norris, J. R. and Lubin, D. (2019) Meteorological Drivers and Large-Scale Climate Forcing of West Antarctic Surface Melt. Journal of Climate, 32(3), 665-684. https://doi.org/10.1175/JCLI-D-18-0233.1.

996

997 Silber, I., Verlinde, J., Wang, S.-H., Bromwich, D. H., Fridlind, A. M., Cadeddu, M., Eloranta, E. W. and
998 Flynn, C. J. (2019) Cloud Influence on ERA5 and AMPS Surface Downwelling Longwave Radiation Biases
999 in West Antarctica. Journal of Climate, 32(22), 7935-7949. https://doi.org/10.1175/JCLI-D-19-0149.1.

1000

1001 Simmonds, I., Keay, K. and Lim, E.-P. (2003) Synoptic Activity in the Seas around Antarctica. Monthly
1002 Weather Review, 131(2), 272-288. https://doi.org/10.1175/1520-0493(2003)131<0272:SAITSA>2.0.CO;2

1003

1004 Smith, B., Fricker, H. A., Gardner, A. S., Medley, B., Nilsson, J., Paolo, F. S., Holschuh, N., Adusumilli,
1005 S., Brunt, K., Csatho, B., Harbeck, K., Markus, T., Neumann, T., Siegfried, M. R. and Zwally, H. J. (2020)
1006 Pervasive ice sheet mass loss reflects competing ocean and atmosphere processes. Science, 368, 1239-1242.
1007 https://doi.org/10.1126/science.aaz5845.

1008

1009 Speirs, J. C., McGowan, H. A., Steinhoff, D. F. and Bromwich, D. H. (2013) Regional climate variability
1010 driven by foehn winds in the McMurdo Dry Valleys, Antarctica. International Journal of Climatology, 33,
1011 945-958. https://doi.org/10.1002/joc.3481.

1012

1013 Stanton, T. P., Shaw, W. J., Truffer, M., Corr, H. F. J., Peters, L. E., Riverman, K. L., Bindschadler, R.,
1014 Holland, D. M. and Anandakrishnan, S. (2013) Channelized Ice Melting in the Ocean Boundary Layer
1015 Beneath   Pine   Island   Glacier,   Antarctica.   Science,   341,   1236-1239.
1016 https://doi.org/10.1126/science.1239373.

1017

1018 Steinley, D. (2006) K-means clustering: A half-century synthesis. British Journal of Mathematical and
1019 Statistical Psychology, 59, 1-34. https://doi.org/10.1348/000711005X48266.

1020

1021 Stigter, E. E., Litt, M., Steiner, J. F., Bonekamp, P. N. J., Shea, J. M., Bierkens, M. F. P. and Immerzeel,
1022 W. W. (2018) The Importance of Snow Sublimation on a Himalayan Glacier. Frontiers in Earth Sciences,
1023 6, 108. https://doi.org/10.3389/feart.2018.00108.

1024

1025 The IMBIE team (2018) Mass balance of the Antarctic Ice Sheet from 1992 to 2017. Nature, 558, 219-222.
1026 https://doi.org/10.1038/s41586-018-0179-y.

1027

1028 Tian, L., Li, H., Li, F., Li, X., Du, X. and Ye, X. (2018) Identification of key influence factors and an
1029 empirical formula for spring snowmelt-runoff: A case study in mid-temperate zone of northeast China.
1030 Scientific Reports, 8, 16950. https://doi.org/10.1038/s41598-018-35282-x.

1031

1032 Turner, J. (2004) The El Nino-Southern Oscillation and Antarctica. International Journal of Climatology,
1033 24, 1-31. https://doi.org/10.1002/joc.965.

1034

1035 Turner, J., Phillips, T., Hosking, J. S., Marshall, G. J. and Orr, A. (2013) The Amundsen Sea low.
1036 International Journal of Climatology, 33, 1818-1829. https://doi.org/10.1002/joc.3558.

1037

1038 van den Broeke, M. R. (1997) Spatial and temporal variation of sublimation on Antarctica: Results of a
1039 high-resolution general circulation model. Journal of Geophysical Research, 102, 29765-29777.
1040 https://doi.org/10.1029/97JD01862.

1042 [Dataset] Vermote, E. (2015a) MOD09CMG MODIS Surface Reflectance Daily L3 Global 0.05Deg CMG.
1043 NASA EOSDIS Land Processes DAAC. http://doi.org/10.5067/MODIS/mod09cmg.006.

1045 [Dataset] Vermote, E. (2015b) MYD09CMG MODIS Surface Reflectance Daily L3 Global 0.05Deg CMG.
1046 NASA EOSDIS Land Processes DAAC. http://doi.org/10.5067/MODIS/myd09cmg.006.

1048 Webber, B. G. M., Heywood, K. J., Stevens, D. P., Dutrieux, P., Abrahamsen, E. P., Jenkins, A., Jacobs, S.
1049 S. , Ha, H. K., Lee, S. H. and Kim, T. W. (2017) Mechanisms driving variability in the ocean forcing of
1050 Pine Island Glacier. Nature Communications, 8, 14507. https://doi.org/10.1038/ncomms14507.

1052 Wiesenekker, J. M., Munneke, P. K., Van den Broeke, M. R. and Smeets, C. J. P. P. (2018) A Multidecadal
1053 Analysis of Fohn Winds over Larsen C Ice Shelf from a Combination of Observations and Modeling.
1054 Atmosphere, 9(5), 172. https://doi.org/10.3390/atmos9050172.

1056 Willie, J. D., Favier, V., Gorodetskaya, I. V., Agosta, C., Kittel, C., Beeman, J. C., Jourdain, N. C., Lenaerts,
1057 J. T. M. and Codron, F. (2021) Antarctic atmospheric river climatology and precipitation impacts. Journal
1058 of Geophysical Research: Atmospheres, 126, e2020JD033788. https://doi.org/10.1029/2020JD033788.

1060 Wingham, D. J., Wallis, D. W. and Shepherd, A. (2009) Spatial and temporal evolution of Pine Island
1061 Glacier thinning, 1995-2006. Geophysical Research Letters, 36, L17501.
1062 https://doi.org/10.1029/2009GL039126.

1064 Yuan, X. (2004) ENSO-related impacts on Antarctic sea ice: a synthesis of phenomenon and mechanisms.
1065 Antarctic Science, 16(4), 415-425. https://doi.org/10.1017/S0954102004002238.

1067 Yuan, X. and Martinson, D. G. (2001) The Antarctic dipole and its predictability. Geophysical Research
1068 Letters, 28, 3609-3612. https://doi.org/10.1029/2001GL012969.

1070 Zhang, X., Wu, B. and Ding, S. (2022) Combined effects of La Nina events and Arctic tropospheric
1071 warming on the winter North Pacific storm track. Climate Dynamics. https://doi.org/10.1007/s00382-022-
1072 06389-9.

1073 Zheng, M. and Li, X., (2022) Distinct patterns of monthly Southern Annular Mode events. Atmospheric
1074 and Oceanic Science Letters, 15, 100206. https://doi.org/10.1016/j.aosl.2022.100206.

1075 Zou, X., Bromwich, D. H., Montenegro, A., Wang, S.-H. and Bai, L. (2021a) Major surface melting over
1076 the Ross Ice Shelf part I: Foehn effect. Quarterly Journal of the Royal Meteorological Society, 147, 2874-
1077 2894. https://doi.org/10.1002/qj.4104.

1078

1079   Zou, X., Bromwich, D. H., Montenegro, A., Wang, S.-H. and Bai, L. (2021b) Major surface melting over
1080   the Ross Ice Shelf part II: Surface energy balance. Quarterly Journal of the Royal Meteorological Society,
1081   147, 2895-2916. https://doi.org/10.1002/qj.4105.
1082
1083   Zou, X., Bromwich, D. H., Nicholas, J. P., Montenegro, A. and Wang, S.-H. (2019) West Antarctic surface
1084   melt event of January 2016 facilitated by fohn warming. Quarterly Journal of the Royal Meteorological
1085   Society, 145, 687-784. https://doi.org/10.1002/qj.3460.
1086